UCLouvain

AGRO LOUVAIN

Faculté des bioingénieurs

Accumulation of Mono-Reduced $[Ir(piq)_2(LL)]^+$ Photosensitizers Relevant for Solar Fuels Productions

Author: **Martin WODON**

Supervisors: **Benjamin ELIAS & Ludovic TROIAN-GAUTIER**

Readers: **Christine DUPONT & Sophie HERMANS**

Academic year 2023–2024

Mémoire de fin d'étude en vue de l'obtention du diplôme de

Bioingénieur : chimie et bio-industries

Acknowledgments

Durant ces deux ans et demi de mémoire, de nombreuses personnes ont contribués à la réalisation de ce travail et je ne pourrais exprimer la gratitude que j'ai envers eux.

Tout d'abord je tiens à remercier le Professeur Benjamin Elias de m'avoir accueilli dans son laboratoire ces deux ans et demi. Je le remercie d'avoir cru en moi et de m'avoir soutenu jusqu'à la fin malgré un parcours un peu particulier. Ce fut un réel plaisir de travailler dans son équipe. Peut-être un peu pour ça que j'ai rallongé mon expérience. Je tiens à lui exprimer ma gratitude pour l'appui qu'il a pu m'apporter tout au long de cette aventure.

Je tiens aussi à remercier Ludovic Troian-Gautier pour son aide et sa disponibilité tout au long de ce mémoire. Il a toujours été là pour répondre à mes questions et avoir de nouvelles idées de projets pour compléter ou approfondir les analyses en cours.

Je souhaite également remercier toute la team de doctorants – Alexia, Martin G, Martin D, Milan et Noémie- pour leur accueil et les réponses aux question sur le fonctionnement ou le emplacements du matériel présent dans le laboratoire. Merci également aux mémorants qui ont travaillé au laboratoire pendant ces deux ans et demi – William et Ulysse.

Mes remerciements vont ensuite à Simon pour tout ce qu'il a pu m'apporter durant ces deux ans et demi. Il a toujours été là pour relire, m'expliquer, analyser des datas,… Je suis heureux d'avoir pu travailler avec lui et je garderai de bons souvenirs de sa bonne humeur qui a rendu ces (nombreuses) heures au laboratoire plus plaisantes. Je suis heureux d'être son premier mémorant à pouvoir rendre et défendre.

J'aimerais aussi remercier la faculté et plus particulièrement la Doyenne Christine Dupont qui m'a toujours montré son soutien et qui m'a permis de finir mon mémoire malgré mon parcours particulier.

Finalement j'aimerais remercier mes parents, ma famille, mes amis et ma copine Manon (qui a en plus passé quelques heures de son temps à relire et corriger ces quelques pages) qui ont tous été très patient durant ces années et qui m'ont soutenu jusqu'au bout.

Abstract

A series of nine $[Ir(piq)_2(LL)]^+.PF_6^-$ photosensitizers were developed and investigated for excited-state electron transfer with sacrificial electron donors that included triethanolamine (TEOA), triethylamine (TEA), and 1,3-dimethyl-2-phenyl-2,3-dihydro-1*H*-benzo[*d*]imidazole (BIH) in acetonitrile. The photosensitizers were obtained in 57-82% yield starting from the common $[Ir(piq)_2Cl]_2$ precursor and were all characterized by UV-Vis absorption as well as by steady-state, time-resolved spectroscopies, and electrochemistry. The excited-state lifetimes ranged from 250 to 3350 ns and were also shown, in some cases, to be strongly influenced by dissolved oxygen. Excited-state electron transfer quenching rate constants in the 10 $M^{-1}s^{-1}$ range were obtained when BIH was used as electron donor. These quenching rate constants were three orders of magnitude higher than when TEA or TEOA is used. Steady-state photolysis in the presence of BIH showed that the stable and reversible accumulation of mono-reduced photosensitizers was possible, highlighting the potential use of these Ir-based photosensitizers in photocatalytic reactions relevant for solar fuels production.

Contents

I. INTRODUCTION 13

1. CONTEXT 13
2. THE ROLE OF HYDROGEN IN A LOW-CARBON TRANSITION AND PRODUCTION PATHWAYS 14

2.1 Hydrogen production streams 14

2.2 Hydrogen's energy density 17

2.3 Use of hydrogen in energy transition 18

3. SOLAR ENERGY TO HYDROGEN 22

3.1 Water splitting 23

3.2 Photocatalyzed hydrogen production system 24

3.3 Catalytic centres 25

3.4 Photosensitizers 25

3.5 Sacrificial electron donor 26

4. ELECTRONIC CONFIGURATION OF $[Ir(N\text{-}C)_2(N\text{-}N)]^+$ COMPLEXES 27
5. EXCITED-STATES PROPERTIES 31

5.1 Photoinduced electron transfer 33

6. ANALYSES OF PHOTOPHYSICAL PROPERTIES FOR FUTURE APPLICATION 35
7. STERN-VOLMER 35
8. MARCUS THEORY 36

8.1 Why study the Marcus curve? 36

8.2 Marcus theory 37

8.3 Diffusion boundary problem 39

II OBJECTIVES AND STRATEGY 41

III RESULTS AND DISCUSSION 42

1 SYNTHESIS 42

1.1 Synthesis of the iridium precursor 42

1.2 Synthesis of $[Ir(piq)_2(LL)]$ 43

2 PHOTOPHYSICS 44

2.1 Absorption spectroscopy 45

2.2 Emission spectroscopy and excited state lifetime 46

2.3 Quantum yields 47

2.4 Excited state lifetime 47

3 ELECTROCHEMISTRY 48

3.1 Differential pulse and cyclic voltammetry 48

3.2 Stern Volmer 50

3.3 Reversibility after accumulation of the mono-reduced photosensitizer 53

3.4 Marcus Curve: Link between thermodynamic and kinetic 54

IV CONCLUSION **57**

V EXPERIMENTAL PART **58**

VI BIBLIOGRAPHICAL REFERENCES **63**

Figures

Figure 1-Reactions in steam reforming of natural gas 15
Figure 2-Different hydrogen production steams 16
Figure 3-different colours assigned to hydrogen 17
Figure 4-Renewable energy to hydrogen to use 18
Figure 5-Fuel cell 20
Figure 6-Simplified scheme of a monocomponent system for H2 photoproduction using a light-harvesting photosensitizer (PS), a reduction catalyst (Cat) and an electron bridge (B)24
Figure 7-homogeneous system with ruthenium-based photosensitizer 25
Figure 8-- reductive quenching in a system with photosensitizer..... 27
Figure 9-LCAO diagram for an homonuclear diatomic molecule 28
Figure 10-Simplified energy diagram for a bis-cyclometalated IrIII complex [Ir(C-N)2(N- N)]+. 29
Figure 11-UV-visible absorption spectrum of $[Ir(ppy)2(bpy)]^{+}$ in acetonitrile at room temperature. 30
Figure 12-Jablonski-Perrin diagram and intramolecular deactivation pathways for a hypothetic molecule. 32
Figure 13-Illustration of oxidation and reduction electron transfer. 33
Figure 14-Differets pathways of a quenching reaction 35
Figure 15-Evolution of the electron transfer kinetics as a function of the reorganization energy and the driving force 39
Figure 16-Marcus' curve observed by Closs and Miller 40
Figure 17-The series of $[Ir(piq)_2(LL)]^{+}.PF_6^{-}$ photosensitizers investigated in the present work. 41
Figure 18-Synthetic scheme for the synthesis of Ir(III) dimers, precursors of the complexes. 42
Figure 19-Synthetic scheme for the synthesis of $[Ir(piq)_2(LL)]$ 43

Tables

Table 1. Photophysical properties of photosensitizers 1-9 recorded in acetonitrile 44

Table 2. Ground and excited-state reduction potentials for photosensitizers 1-11 50

Table 3. Driving force (ΔG) and quenching rate constants (kq) for electron transfer between BIH, TEOA or TEA and excited photosensitizers 1-9.a 52

List of abbreviations

bpy	2-2'-Bipyridine
B	Bridge
CCS	Carbon capture and storage
Cat	Catalyst
°C	Celsius degree (temperature unit)
CT	Charge Transfer
COP21	21st Conference of the Parties
CB	Conduction Band
BIH	1,3-dimethyl-2-phenyl-2,3-dihydro-1H-benzo[d]imidazole
d	Doublet
e^-	Electron
eV	Electron Volt
eq	Equivalent
ES	Excited State
g	Gram (Mass unit)
g/mol	Gram per mol
GHG	Greenhouse gases
GS	Ground State
HOMO	Highest Occup ied Molecular Orbital
h	Hours
HER	Hydrogen evolution reaction
IR	Infrared
IPCC	Intergovernmental Panel on Climate Change
IC	Internal Crossing
ISC	Inter System Crossing
IEA	International Energy Agency
Ir	Iridium
kcal/mol	Kilocalorie per mol
kJ	Kilojoules
LLCT	Ligand to Ligand Charge Transfer
LMCT	Ligand to Metal Charge Transfer

LC	Ligand Centred
hν	Light
L	Litre (volume unit)
LUMO	Lowest Unoccupied Molecular Orbital
MS	Mass Spectrum
MC	Metal Centred
MOx	Metal Oxide
MLCT	Metal to Ligand Charge Transfer
mmol	Millimole (quantity of matter unit)
mL	Millilitre (volume unit)
min	Minutes
MO	Molecular Orbital
nm	Nanometre
NOx	Nitrogen oxides
NHE	Normal Hydrogen Electrode
NMR	Nuclear Magnetic Resonance
ppm	Part per million (NMR unit shift)
PS	Photosensitiser
Piq	Phenylisoquinoline
ps	Picosecond
PWh,MWh	Petawatt-hours, megawatt-hours
Ex/x	Potential
pH	Potential of Hydrogen
UV	Ultra-Violet
UNFCCC	United Nations Framework Convention on Climate Change
SD	Sacrificial electron donor
s	Singlet
TER	Train express régional
TOF	Turnover frequency
TON	Turnover number
TEOA	Triethanolamine
TEA/ Et_3N	Triethylamine
t	Triplet

ZEHS Zero Emission Haulage Solution

I. Introduction

1. Context

In 2015 in Paris, at the 21st Conference of the Parties (COP21) to the United Nations Framework Convention on Climate Change (UNFCCC), the international community adopted a global climate agreement. This agreement, known as the "Paris Agreement", sets an ambitious and robust framework for international climate action for decades to come. It aims to reduce greenhouse gas (GHG) emissions to limit the rise in global average temperature below 2°C above pre-industrial levels, with a target of no more than 1.5°C[1].

Limiting warming to 1.5°C implies reducing global greenhouse gas emissions by about 45% in 2030 compared to 2010 and reaching net zero emissions by 2050[1]. This requires rapid and far-reaching systemic transitions in energy, urban, industrial, and land-use systems, as well as a significant increase in investments. Any further delay in mitigation action could lead to a 1.5°C increase in global warming.

The Intergovernmental Panel on Climate Change (IPCC) report of 2022 on climate change mitigation states that reducing emissions from the energy sector requires major transformations. This includes a substantial reduction in the use of fossil fuels, deployment of low-emission and carbon-free energy sources, switching to alternative energy carriers, efficiency, and conservation of energy resources.[2] Continued installation of fossil fuel-based infrastructure (without carbon capture and storage (CCS)) will lead to greenhouse gas emissions in the future. Carbon neutrality in the industry can be achieved through the transformation of production processes, circularity of material flows, demand management, and the use of decarbonized energy sources and carriers.

2. The role of hydrogen in a low-carbon transition and production pathways

Hydrogen can be a key vector in the transition to a low-carbon future. Indeed, molecular hydrogen is a gaseous compound that can act as an energy carrier and can be used as a fuel that can be stored and moved to deliver energy. When used as an energy source, its combustion only releases water as a side product and is therefore considered essential for decarbonizing processes. According to McKinsey, it is estimated that up to 25% of global emissions could be reduced by using hydrogen by 2050. Hydrogen is also expected to make a significant contribution to decarbonizing specific industrial sectors, such as iron and steel production, the chemical industry and heavy transport. With current industrial uses of hydrogen focused on oil refining and ammonia production, the Hydrogen Council and McKinsey estimate that the use of hydrogen could avoid up to 270 million tons of CO_2 per year and 90 million tons of CO_2 in transport and mobility alone.[3]

Beyond reducing emissions as a key feature of hydrogen production, it can also bring resilience to countries seeking energy independence and diversification, thanks to the fact that it can be produced locally from multiple feedstocks using different production routes.

But how is hydrogen produced today? At present, there are three main production methods (other production streams exists as well).

2.1 Hydrogen production streams

The first of these three is steam reforming of natural gas. This is the most common technique. This involves reacting methane with water to obtain a mixture containing hydrogen and CO_2 (**Figure 1**).[4] The CO_2 emitted by this process could eventually be captured and stored to produce decarbonized hydrogen.[5] Instead of natural gas, the use of biomethane (methane from the fermentation of biomass) is also a solution for producing low carbon hydrogen.

Reactions	Reaction description	Standard enthalpy of reactions [kJ·mol^{-1}]	
$CH_4 + H_2O \rightleftharpoons CO + 3H_2$	Steam reforming	206	R①
$CO + H_2O \rightleftharpoons CO_2 + H_2$	WGS	-41	R②
$CH_4 + CO_2 \rightleftharpoons 2CO + 2H_2$	CO_2 reforming	247	R③
$C_nH_m + nH_2O \rightleftharpoons nCO + \left(\frac{m}{2} + n\right)H_2$	Higher hydrocarbons steam reforming	1175*	R④

*[Standard conditions at $P = 1$ atm, $T = 298$ K, for n-C_7H_{16}].

Figure 1-Reactions in steam reforming of natural gas [6]

Secondly, hydrogen can also be produced from water and electricity by a process called water electrolysis (**equation 1**). The electrolyser separates a water molecule into hydrogen and oxygen. This method is still not very widespread because it is much more expensive (2 to 3 times more expensive than natural gas reforming) and is currently reserved for specific uses, such as electronics, which require a high level of purity for hydrogen.[7]

$$H_2O \rightarrow H_2 + \tfrac{1}{2}\, O_2 \quad E=1.23V \quad Eq.1$$

The last technique is gasification which produces, by combustion, a mixture of CO and H_2 from coal (a solution that emits a lot of CO_2) or biomass.[8,9] A diagram of different production-to-use steams are shown in **Figure 2**.

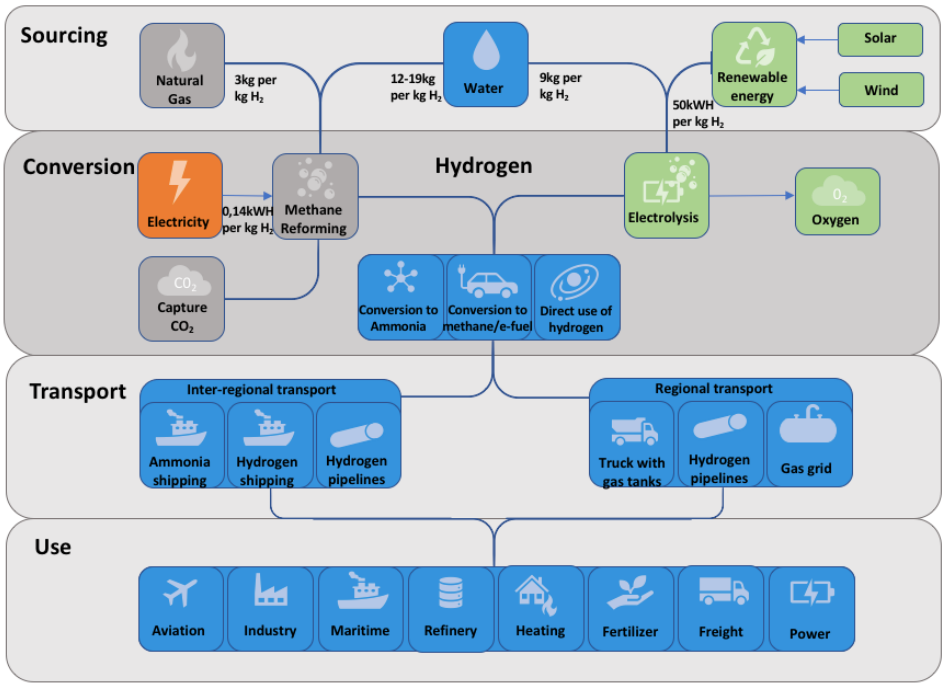

Figure 2-Different hydrogen production-to-use steams

Depending on the method of production, hydrogen is given a "colour".[10] This colour is of course fictitious and not real. There are five different colours also described in **Figure 3**:

1. Green hydrogen, which is made by electrolysis of water using electricity coming only from renewable energy.
2. Grey hydrogen, which is manufactured by thermochemical processes using fossil fuels (coal or natural gas) as raw materials.
3. Blue hydrogen, which is manufactured in the same way as grey hydrogen, with the difference that the CO_2 emitted during manufacture is captured for reuse or storage.
4. Purple hydrogen, which is more specific to France, is made by electrolysis like green hydrogen, but the electricity comes from nuclear energy.
5. Turquoise hydrogen, which is made by pyrolysis of natural Gas, which produce hydrogen and pure carbon.

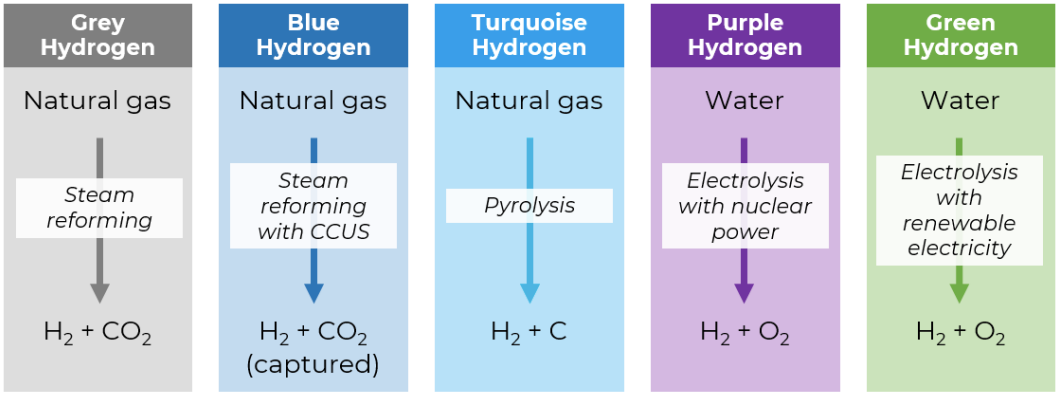

Black, brown, white, yellow and orange hydrogens also exist...

Figure 3-different colours assigned to hydrogen[11]

2.2 Hydrogen's energy density

As for storage, although hydrogen (H_2) has a very high mass density of energy (1 kg of hydrogen contains as much energy as about 3 kg of oil), it has a very low volume density. Therefore, it must be transformed to be able to store it in a usable volume. Under atmospheric conditions, hydrogen is gaseous and therefore takes up a lot of space and has a low energy density (10,8 kJ/L). On the other hand, by compressing it, we can make the gas denser, or even liquid, and so transport and store more of it in a smaller volume. This implies an increase in its energy density. By way of comparison, by compressing it to 700 bar, 7 litres of hydrogen can contain as much energy as 1 litre of petrol. Petrol and diesel carry between 8.8 and 10 kWh/L, respectively, and pressurised hydrogen contains about 0.5 kWh/L at 200 bar, 1.1 kWh/L at 500 bar and 1.4 kWh/L at 700 bar. By liquefying it to compress it further at a temperature of -253°C, 4 litres of liquid hydrogen would then contain the equivalent energy of 1 litre of petrol. Densifying hydrogen makes it possible to operate at lower pressures but requires more energy, which makes it more expensive. [12,13,14]

Hydrogen is usually transported in compressed form via a relatively extensive pipeline network, with a total of over 4,500 km worldwide, including 1,600 km in Europe and 2,500 km in the U.S. Countries such as Japan are also considering importing hydrogen, which would then be transported by ship from Australia, for example.[15]

2.3 Use of hydrogen in energy transition

Currently, hydrogen has two main uses: as a feedstock to produce ammonia (fertiliser) and methanol, and as a reagent in the process of refining crude oil into petroleum products, fuels and biofuels. The possible uses are nevertheless numerous, and hydrogen, as mentioned above, is promising for decarbonising several sectors and accompanying the energy transition. In this idea, recovering energy from previously stored renewable or low-carbon dihydrogen is done in two ways: either in the form of heat via its direct combustion with oxygen, or in the form of electricity via a fuel cell. In both cases the overall reaction produces only water and the energy produced can be used in various ways. Hydrogen has been assigned three essential objectives to make a success of the energy transition: decarbonizing transport, storing electricity and injecting it into the networks, and decarbonizing the industrial sector (**Figure 4**).[12,13,16,17]

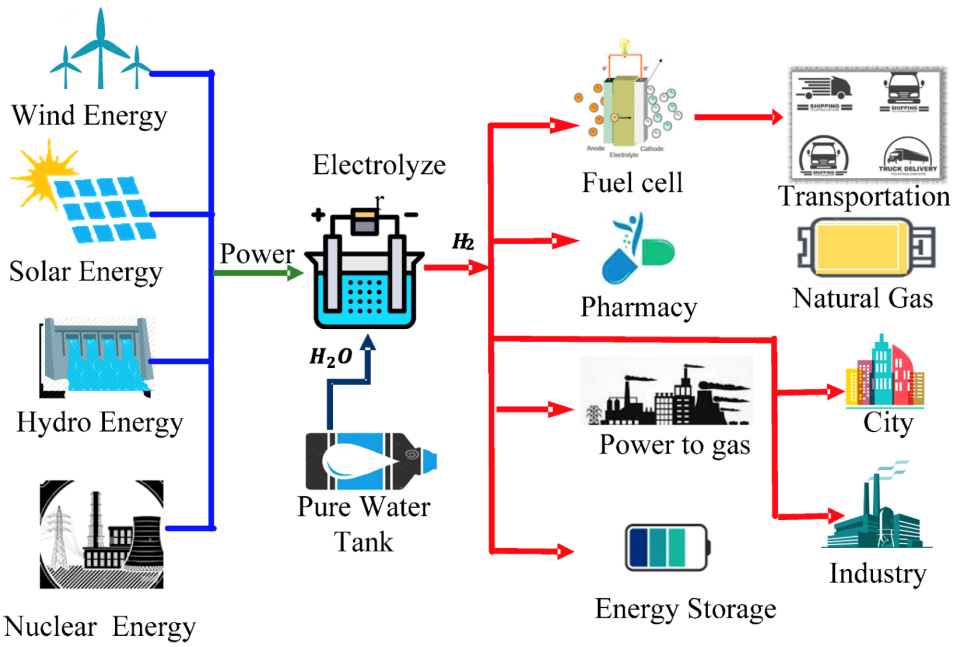

Figure 4-Renewable energy to hydrogen to use [17]

2.3.1 Hydrogen in transport

There are three notable transportation means for which hydrogen can be used: cars and trucks, trains, and planes.

Firstly, for cars and trucks, hydrogen can be used in two ways: in ignition engine or in fuel cell. The first is as fuel in a "petrol" type spark ignition engine. The main advantage lies in the environmental balance: combined with oxygen, the combustion of hydrogen produces mainly water and heat and only nitrogen oxides (NOx)(due to the presence of N_2 in the air). However, this solution requires specific adaptations to achieve very high efficiency and very low NOx emissions. It is necessary to exploit various properties of hydrogen, such as its ability to burn rapidly in a very clean mixture. The use of hydrogen in an internal combustion engine can benefit from the latest advances in the combustion engine and from coupling with a hybrid powertrain. Thus, based on more robust and mature technologies than those currently used for fuel cells, it would be possible to achieve efficiencies of over 50%. This could be a transitional solution to the fuel cell (see below), as it allows the validation of the entire hydrogen production and distribution chain to begin using existing industrial production tools.[13,15,16]

The second way is to use hydrogen in a fuel cell. In the long term, car manufacturers are also interested in fuel cells as electricity generators for electric vehicles. This is to complement battery-powered electric vehicles, which currently suffer from limited range and recharging time. Hydrogen is then used to power a fuel cell - which produces electricity - to enable the electric motor that drives the vehicle to function. Hydrogen is one of the best energy carriers for fuel cells today in terms of energy performance and emissions. Their overall efficiency is above 50% over a wide operating range, which is an attractive advantage over a current petrol engine. Fuelled by a mixture of air and hydrogen, the battery converts the chemical energy of hydrogen into electrical energy using the reverse principle of electrolysis as shown in the **equation 2** below.[14,16]

$$H_2O \rightarrow H_2 + \tfrac{1}{2}\, O_2 \quad E=1.23V \quad \text{Eq.2}$$

By reacting hydrogen with oxygen from the air on the electrodes (thin membranes covered with a platinum-based catalyst), fuel cells produce electricity without any emissions other than water vapor (**Figure 5**). The fuel cell effect was discovered by German scientist Christian Schönbein in 1839[18].

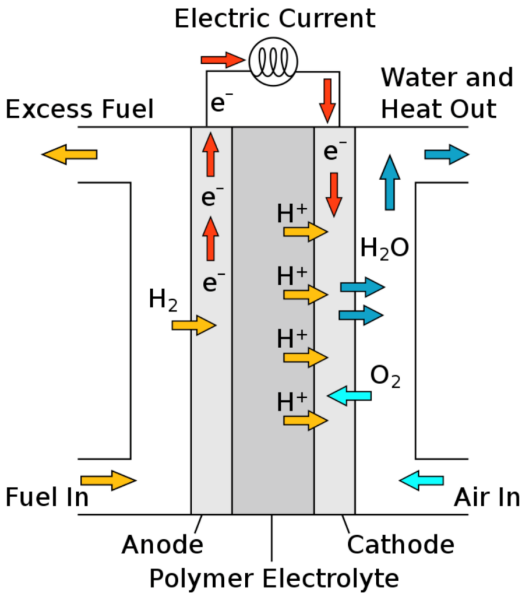

Figure 5-Fuel cell [18]

For trains and aircraft, many projects are emerging. For example, the French hydrogen plan includes among its objectives the introduction of the first hydrogen train in France. After Germany, France is taking its first steps in hydrogen rail mobility. The SNCF and the Regions, which have launched the TER H2 project (brand name used by SNCF for regional express transport), which aims to set up the very first fleet of regional hydrogen trains in several pilot French regions, have also carried out the first journeys on the open network in France, from the 1st to 3rd of February 2023, on the Tours-Loches line with hydrogen Coradia trains. These operations were conducted by the manufacturer Alstom and the Centre-Val de Loire region. These trains, which also run on a fuel cell, are intended to eventually replace trains that still run on diesel. Diesel still accounts for 26% of the energy consumed by TER and is responsible for 77% of the company's CO_2 emissions. Twelve hydrogen trains have already been ordered. They are due to enter commercial service at the end of 2025.[19]

As for the hydrogen aircraft or "clean aircraft", while it is already giving rise to ambitious projects, it still must answer several questions in terms of technology, environment and safety. The use of hydrogen in aviation has many advantages. Indeed, as mentioned above, hydrogen has a very high mass density energy, so for the same amount of energy, it requires less weight. Compared to other potential electric planes, it is a much faster refuelling than recharging a batterie.[15,16]

2.3.2 Hydrogen in energy storage

A second essential objective is to store electricity and injecting it into the networks. The storage of energy in the form of hydrogen makes it possible to compensate for the intermittence of renewable energies (wind and solar) by optimizing electricity production capacity. In the context of the development of a renewable electricity mix, electrolysis makes it possible, when the network is in surplus (i.e., when electricity production exceeds consumption), to store hydrogen for a short or long period of time, depending on requirements. In the case of a network deficit, the available hydrogen can be reused in a fuel cell to produce electricity.[16]

Hydrogen can also be injected directly into gas networks either by direct injection into gas networks for combustion or by producing synthetic methane (according to the principle of methanation): conversion of CO or CO_2 in the presence of hydrogen, which can then be transformed into heat, electricity, or fuel.[15]

2.3.3 Hydrogen in industrial processes

The third key objective is the role of decarbonisation of industry. Today, according to the International Energy Agency (IEA), industry accounts for 29% of final energy consumption and 37% of global CO_2 emissions.[20] Hydrogen can be used in the industrial sector on the one hand to supply decarbonised energy to the industrial units concerned, and on the other hand to contribute to the decarbonisation of the industrial processes concerned by replacing the fossil fuels currently used. This is the case, for example, in the manufacture of steel, which results from the reduction of iron ore. This reduction, which is carried out today using coal, could be carried out tomorrow using decarbonised hydrogen.

2.3.4 Example of a case study of the use of hydrogen

On May 6th of 2022, Engie and Anglo American, one of the world's largest mining players, jointly inaugurate the Rhyno project, as part of the nuGen™ program, developed for the Mogalakwena platinum mine in South Africa.[21] They developed the prototype of the world's largest hydrogen-powered mining truck, capable of carrying a 290-ton payload. There is an integrated hydrogen solution, including production, compression, storage, and refuelling in

record time. Once validated, this "proof of concept" should be extended to other sites. The objective is to reduce diesel emissions from mining mobility by up to 80%.

This truck, which can transport 290 tons, runs on a hydrogen-powered battery with a capacity of 2 megawatts. It generates more power than equivalent diesel models. The truck has a 1.2 MWh battery pack consisting of several cells with a capacity of 800 kW each.

The new truck draws its energy from a solar panel farm that supplies a hydrogen electrolyser. This is part of the NuGen ZEHS (Zero Emission Haulage Solution) system being implemented at the mine. The project is due to start in 2026, and is a very important piece of the jigsaw that will enable Anglo American's eight mines to be carbon-neutral by 2030 (2040 for the group's entire operations).
This initiative will be closely watched by other mining companies, which are under pressure to improve their carbon footprint. Hydrogen is clearly part of the solution for these traditionally high-polluting companies.

In the program presented above, the plan is to use undeveloped land to install solar panels, generate electricity and produce hydrogen using an electrolyser. Nonetheless, if the intermediate stage could be avoided and hydrogen could be produced directly from solar energy, it would avoid losses associated with this intermediate step.

3. Solar energy to hydrogen

To meet future hydrogen needs, it is necessary to find other streams of production than those shown in **Figure 3**. Indeed, the transformation of electricity from renewable energies into hydrogen seems interesting to fluidify production variations, but the losses linked to a double transformation (electricity-hydrogen-electricity) with the current electrolysers and fuel cells are high. Indeed, the efficiency of an electrolyser is between 60 and 75%, and the efficiency of fuel cells is currently 50%. The overall efficiency is therefore around 35% [22], which is still relatively low. Avoiding too many intermediaries, therefore, seems to be an interesting option. Among the energy sources, the sun seems to be the most promising. The amount of energy received by the Earth is considerable. Every year, the Earth receives 1,070,000 petawatt-hours (PWh, or 10^{15} Wh), which is more than 9,000 times the world's annual energy consumption (116 PWh in

2019 according to the International Energy Agency (IEA))[23]. Exploiting only 0.0001% of this energy would therefore be enough to cover the planet's energy demand.

3.1 Water splitting

One method of converting solar energy that has been studied extensively and on which many hopes are based is “water splitting”. This is a process that results in the dissociation of hydrogen and oxygen from water as a result of an external energy input (**equation 3**). The balance of the decomposition of a water molecule is as follows:

$$H_2O \rightarrow H_2 + \frac{1}{2} O_2 \quad E=1{,}23V \quad \Delta_r G^0 = 241kJ \; Eq.3$$

It is established, for one mole of water:
Since the water molecule H_2O consists of two O-H bonds, each of which has a molar energy of 460 kJ, breaking them absorbs 2 × 460 = 920 kJ. The reassembling of the gaseous dihydrogen molecules produces an energy input: $2\,H \rightarrow H_2$ + 432 kJ ;
The reassembling of oxygen releases: $2\,O \rightarrow O_2$ + 494 kJ, so 247 kJ per mole of initial water.
The overall balance is therefore an absorption of:

$$920kJ - 432kJ - 247kJ = 241 \text{ kJ Eq.4}$$

Thus, the production of two grams of hydrogen by cracking one mole of water (without taking losses into account) requires the input of 241 kJ, and 120,500 kJ to produce 1 kg of hydrogen or 33.5 kWh/kg of hydrogen.

The overall splitting of water is generally difficult to achieve due to the bottom-up nature of the reaction. The redox process is separable into two half-reactions: the reduction of two protons to H_2 (**equation 5**) and the oxidation of water to O_2 (**equation 6**) with a flow of electrons between the two processes.

$$2H^+ + 2e^- \rightarrow H_2 \; Eq.5$$

$$H_2O \rightarrow {}^1\!/_2\, O_2 + 2H^+ + 2e^- \; Eq.6$$

3.2 Photocatalyzed hydrogen production system

In this work, we mainly focused on the photocatalyzed hydrogen evolution reaction (HER). The main feature of our systems is based on charge separation: each absorbed photon leads to the transfer of an electron in a given direction (**Figure 6**). This is achieved by a potential difference between the catalyst and the photosensitiser. The main components of these photochemical hydrogen evolution systems are a photosensitiser (PS) that captures the light, a proton reduction catalyst (Cat) and an electron bridge (not necessary) (B) that connects them (**Figure 6**). A sacrificial electron donor such as EDTA, Et_3N, triethanolamine (TEOA), sodium ascorbate... is therefore needed to regenerate the oxidised photosensitiser.[24] These sacrificial donors are therefore substitutes for H_2O. This regeneration of the photosensitizer is key parameter to allow efficient hydrogen generation.

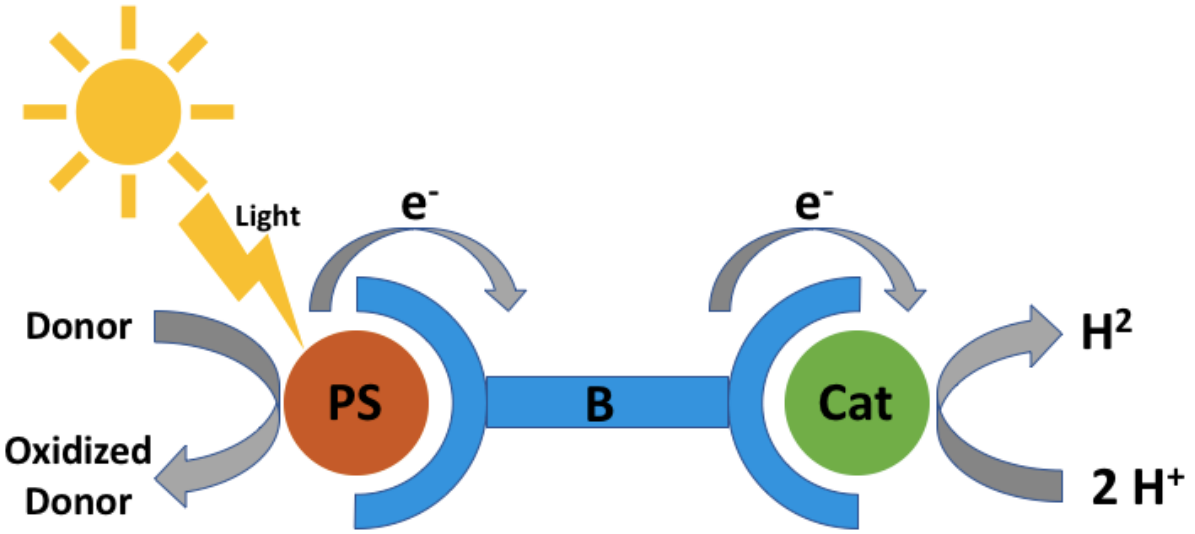

Figure 6-Simplified scheme of a monocomponent system for H2 photoproduction using a light-harvesting photosensitizer (PS), a reduction catalyst (Cat) and an electron bridge (B)

In the literature, several H_2 photoproduction systems based on transition metal complexes such as ruthenium[25], osmium[26] or iridium[27] as photosensitisers and platinum[28], cobalt[29] or palladium[29] as catalytic centres have been studied. Their potential to produce dihydrogen is characterized by two main characteristics, namely the turnover number (TON), defined as the number of moles of substrate that one mole of catalyst can convert before becoming inactivated, and the turnover frequency (TOF) corresponding to the number of revolutions of the catalytic cycle per unit of time.

As catalytic centres for proton reduction are already well studied (green part in the **Figure 6**), and the feasibility of this part of the reaction is no longer in doubt, we studied only photosensitisers (red part in the **Figure 6**) although it would be interesting to test the whole reaction chain in the future.

3.3 Catalytic centres

Even though it is not specifically studied here, it is worth briefly mentioning and explaining these catalytic centres. The best-performing catalysts to date are made of platinum, a rare and expensive noble metal, which makes the process too costly for industrial use. It was therefore necessary to develop alternative catalysts, made from non-noble metals, that would be just as effective in synthesizing hydrogen. Cobalt quickly emerged as a good alternative. In the literature, a certain number of studies about cobalt as a catalytic centre for H_2 production can be found. For example, Xie et.al have achieved good results by designing a catalytic complex based on cobalt and a special ligand, phthalocyanine (**Figure 7**). This homogeneous system was tested with a ruthenium-based photosensitizer and triethylamine (TEA) as a sacrificial electron donor. The system gives up to 2400 TON versus the catalyst with an initial TOF as high as 680 TON h^{-1}.[30]

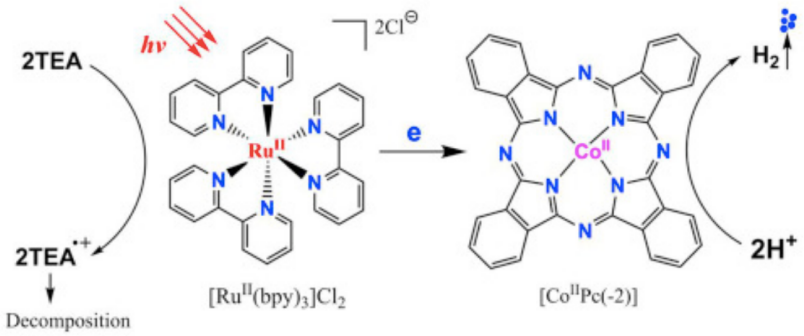

Figure 7-homogeneous system with ruthenium-based photosensitizer [30]

3.4 Photosensitizers

As mentioned above, different transition metals can be good candidates. However, in this master thesis, we focused our efforts on Iridium (Ir) (III) complexes. Since the beginning of the 21st century, Ir(III) compounds have emerged as promising candidates for various

applications (OLED for example), but especially for photoredox catalysis. The success of Ir(III) complexes has made its way into the world of research thanks to several properties. Indeed, it has relatively long-lived excited states and exceptional photo- and redox stability (concepts explained in the following chapter). But if we were to retain the main asset of these complexes, it would certainly be their ability to accommodate up to three cyclometalated (Ir-C) bonds, which offers many tunability options. The number of Ir-C bonds influences the frontier orbitals of the complex due to the difference in σ-donation ability between the Ir-C and Ir-N bonds. Among the combinations of cyclometalated and polypyridine ligands, $[Ir(N\text{-}C)_2(N\text{-}N)]^+$ appears to be of great interest as it allows the independent tuning of the HOMO energy (modifying the C^N ligand) and the LUMO energy (by modifying the N^N ligand). Thus, the HOMO-LUMO gap can then be finely tuned to control the reactivity of the photosensitizers towards photoinduced oxidation and reduction processes.[29]

The modus operandi of a TCS (three-component system) is the following: upon light absorption, PS is promoted to its excited state and acquires at the same time enhanced, in our case, reductive power (can be oxidative power). Thermodynamically speaking, $E(PS^*/PS^-)$ is superior to $E(PS/PS^-)$, i.e. $(E(PS^*/PS^-) = E(PS/PS^-) + E_{00}$, where E_{00} is the lowest excited state energy, and PS* is therefore more prone to harvest an electron from the nearby donor, here a sacrificial electron donor (SD) (**equation 7**).[31]

$$PS^* + SD \rightarrow PS^- + SD^+ \quad \text{Eq.7}$$

In this case, PS ends up in a reduced state, which is why quenching of PS* by an electron donor is referred to as “reductive quenching” (RQ).

3.5 Sacrificial electron donor

In the **equation 7**, the PS is quenched by an electron donor mentioned as a sacrificial electron donor. The sacrificial electron donor (SD) is a simple molecule that is mandatory to drive photo-induced reactions aiming at producing high-added value molecules by photo-induced reduction of low energy value substrates (**Figure 8**). Tertiary aliphatic amines are probably the most used sacrificial donors to fuel photochemical reduction reactions. This class of molecules is epitomized by well-known triethylamine (TEA) and triethanolamine (TEOA). Both were employed in the pioneering works setting the bases for a TCS, with the general

purpose of photo-producing hydrogen gas or photo-decomposing CO_2. TEA and TEOA display very similar features: they exhibit irreversible oxidation potentials around 0.7 V vs. SCE making them thermodynamically able to be part of similar electron transfer processes.[31]

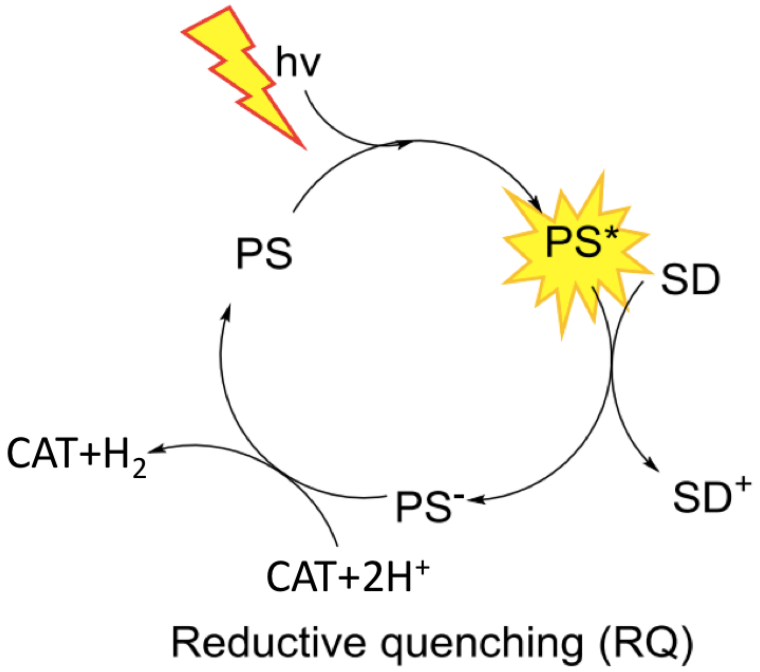

Figure 8-- reductive quenching in a system with photosensitizer[31]

4. Electronic Configuration of $[Ir(N\text{-}C)_2(N\text{-}N)]^+$ Complexes

For a better understanding of the last section, it is relevant to further detail the theory of LCAO (linear combination of atomic orbitals). This theory is based on the study of the energy of the orbitals associated with a group of atoms. It allows the orbitals to be modelled at the scale of the molecule. Transition metal complexes are compounds formed because of coordination bonding between one or more mono- or polydentate ligands and an atom from block d of the periodic table. These bonds result from the sharing of electron doublets present at the coordination sites of the ligands with the metal ion which has empty d orbitals. Thus, following the LCAO theory, the complexation of ligands on a metal ion comes from the formation of molecular orbitals by linear combination of the molecular orbitals of the ligands with the atomic orbitals of the central metal atom (Iridium (III) in our case). Molecular orbitals and the atomic orbitals that give rise to them are represented in linear combination on the same schematic

energy diagram. For example, for homonuclear diatomic molecules built from the first elements of the second period, the diagram looks like the **Figure 9**.[32]

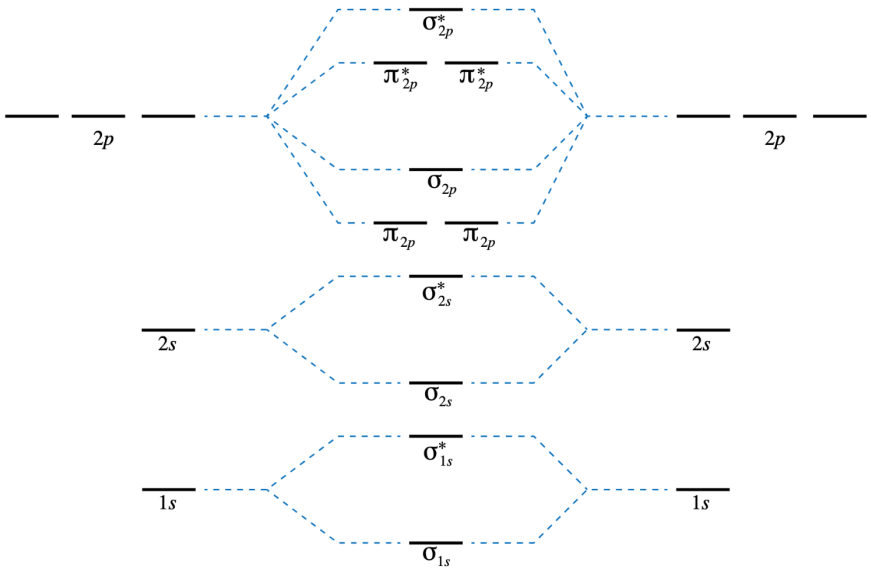

Figure 9-LCAO diagram for an homonuclear diatomic molecule [32]

The Valence Bond Theory fails to answer certain questions like why He_2 molecule does not exist and why O_2 is paramagnetic. Therefore in 1932 F. Hood and R.S. Mulliken came up with Molecular Orbital Theory to explain questions like the ones above. According to the Molecular Orbital Theory, individual atoms combine to form molecular orbitals. Thus, the electrons of an atom are present in various atomic orbitals and are associated with several nuclei.[33]

We know that we can consider electrons as either particle or wave nature. Therefore, we can describe an electron in an atom as occupying an atomic orbital, or by a wave function Ψ. These are solutions to the Schrödinger wave equation. Electrons in a molecule occupy molecular orbitals.

In the case of ML_6 compounds, the mixing of the atomic orbitals of the metal with the molecular orbitals of the ligands leads to various molecular orbitals centred both on the metal and on the ligand. The energy levels associated with these are shown in the **Figure 10**. Among the 6 molecular orbitals presented, 3 are of lower energy and are said to be bonding (σ_L, π_L, π_M), while the other 3 are of higher energy and are said to be anti-bonding ($\sigma_M^*, \pi_L^*, \sigma_M^*$). Among these different molecular orbitals, two of them are of particular interest in the case of

absorption and emissions processes, the LUMO (Lowest Unoccupied Molecular Orbital) and the HOMO (Highest Occupied Molecular Orbital).[34]

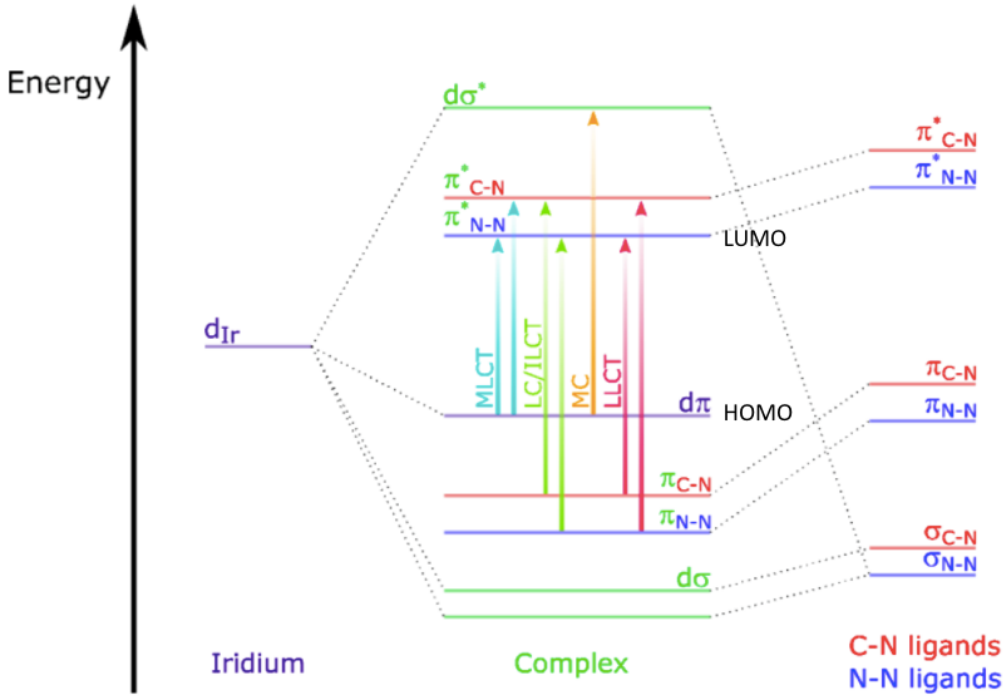

Figure 10-Simplified energy diagram for a bis-cyclometalated IrIII complex [Ir(C-N)2(N- N)]+. [34]

Based on the diagram above, it is possible to deduce the different types of electronic transition between orbitales when the resulting complex is subject to excitation by photon.[34] If the energy of the photon is sufficient, an electron from an orbital of energy less or equal to the HOMO, is then be transferred to an unoccupied orbital of higher energy. These transitions are classified following their orbitals involved:

- LC (Ligand Cantered): this transition implies the transfer of one electron from the orbital π_l to the non-bonding orbital π^*_l of the same ligand (l stands for "ligand") and can be observed in the near-UV region.

- MC (Metal Cantered): this transition implies the transfer of one electron from the orbital $d\pi_m$ to the non-bonding orbital $d\pi^*_m$ of the metal centre (m stands for "metal"). Due to the high energy of the non-bonding orbital, this transition usually lies in the UV range and the return of the electron to the ground state is not emissive

- CT (charge transfer): this reaction implies a change in the oxidation state of the metal and the Ligand resulting from "internal" electron transfer. There are two possible charge transfer processes:

    - MLCT (Metal-to-Ligand Charge Transfer): this transition implies the transfer of one electron from the orbital $d\pi_m$ of the metal centre to the non-bonding orbital π^*_l of a ligand. MLCT results in oxidation of the metal centre and reduction of a ligand implying a change in the polarity of the complex due to charge separation process.
    - *LLCT* (*Ligand-to-Ligand Charge Transfer):* this transition implies the transfer of one electron from the orbital π_l to the non-bonding orbital π^*_l of the different ligand implying, as observed for MLCT, a charge separation within the complex.

These transitions are visible in different regions of the emission spectrum as shown in **Figure 11**.

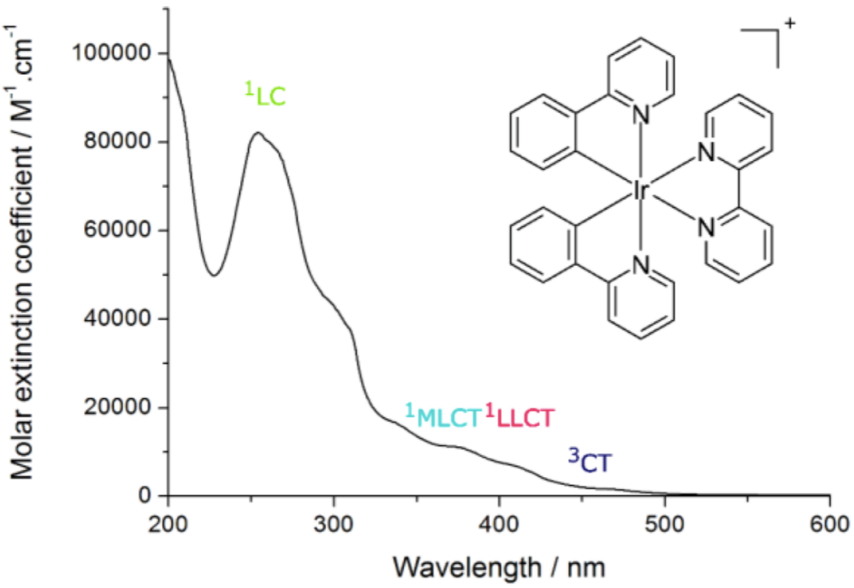

Figure 11-UV-visible absorption spectrum of [Ir(ppy)2(bpy)]⁺ in acetonitrile at room temperature.[34]

$[Ir(ppy)_2(bpy)]^+$ complexes have been part of many research because they possess spatially separated frontier orbitals. This is interesting to study because it enables the independent tuning of HOMO and LUMO levels.

Bis-cyclometalated Ir(III) complexes show a high versatility of their photo- and electrochemical properties. By changing the chemical structure of the different ligands, it is possible to tune their absorption and emission colours. But in addition to that, the oxidation and reduction potentials are also strongly impacted by the modification of the ligands. Usually, electron-withdrawing groups stabilize the HOMO and the LUMO whereas electron-donating groups destabilize them. As an example, the widely accepted paradigm to achieve lower energetic wavelength absorption, the HOMO can be destabilized with electron-donating groups located on the phenyl ring of the C^N ligands and the LUMO be stabilized with electron-withdrawing groups located on the ancillary N^N ligand. The most used electron-withdrawing groups used are fluorine atoms.[35]

5. Excited-States Properties

Following the promotion of an electron in a vacant orbital of higher energy after the absorption of a photon, different types of phenomena can occur to dissipate the stored energy and thus make the complex go back to its fundamental energy state. All these phenomena can be illustrated in a Jablonski diagram (**Figure 12**) in which a multitude of energy levels through which the molecule studied can pass are represented. Initially the molecule is in the singlet ground state (two paired electrons of antiparallel spin) represented by the symbol S_0. The absorption of a photon leads to the formation of an excited state of type S_n (n=1,2,3,...), which itself can lead to a triplet excited state T_n by inter-system crossing (ISC) favoured by heavy atom effect.

The complex in the ground state S_0 is excited to a S_n state. Only these transitions are allowed due to the selection rules that prevent the change of multiplicity of the complex during the transition to the excited state. The complex once excited returns very quickly to the S1 state by non-radiative deactivation such as vibrational relaxation or internal conversion (IC).[29]

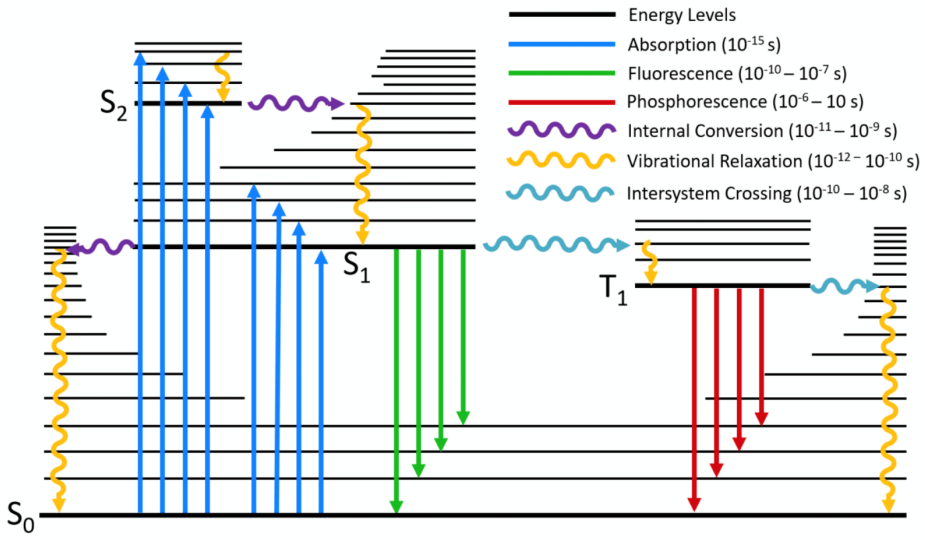

Figure 12-Jablonski-Perrin diagram and intramolecular deactivation pathways for a hypothetic molecule. [36]

From this excited state S1, three phenomena compete:

- A non-radiative relaxation in the form of an internal conversion bringing the molecule back to its fundamental level S_0.
- A radiative relaxation with the emission of a photo of energy corresponding to the energy difference between S_1 and S_0. This is referred to as fluorescence.
- A non-radiative relaxation in the form of an intersystem crossing leading to a Triplet T_1 state of lower energy than S_1. This transition, theoretically forbidden, can however be observed thanks to spin-orbit coupling.

Finally, from this last T_1 state, two types of relaxations can be envisaged, the dominance of one over the other varying according to environmental parameters such as the presence of oxygen, the temperature, or the viscosity of the medium.

- Spontaneous non-radiative relaxation following collisions with the surrounding molecules.
- A radiative relaxation termed phosphorescence.

Fluorescence or phosphorescence processes can only take place from the S_1 or T_1 state respectively. This is the Kasha rule (Kasha, 1950). Finally, the term luminescence is often used

when the photon emission comes from both the fluorescence and phosphorescence processes or when an uncertainty remains on which process really happens upon radiative decay back to the ground state.

5.1 Photoinduced electron transfer

Photoinduced electron transfer is often responsible for luminescence inhibition. This process is involved in many photochemical reactions. It plays an important role in photosynthesis and in artificial systems for solar energy conversion based on charge separation.

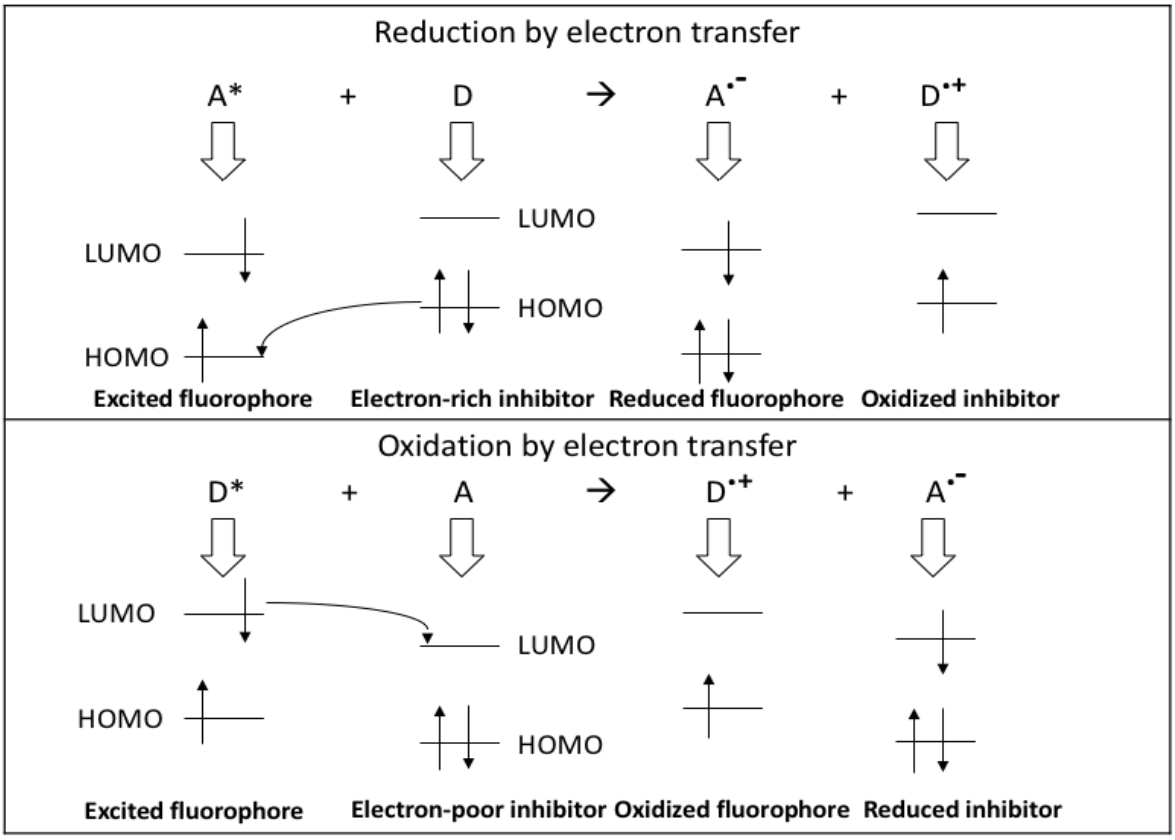

Figure 13-Illustration of oxidation and reduction electron transfer.

A photo-induced electron transfer (PET) is a photochemical process involving the transfer of an electron between a donor (D) and an acceptor (A). This transfer can be oxidative (**equation 8**) or reductive (**equation 9**) depending on which molecule is excited (**Figure 13**).[34]

$$D^* + A \rightarrow D^{\cdot+} + A^{\cdot-} \quad \text{Eq.8}$$

$$A^* + D \rightarrow A^{\cdot-} + D^{\cdot+} \quad \text{Eq.9}$$

These redox reactions occur exclusively under light excitation and are not thermodynamically favoured when molecules are in their ground state. Upon irradiation, a compound becomes a better electron donor (reductant) and acceptor (oxidant). This phenomenon arises from the excess of energy stored after light excitation and leads to an enhancement of the redox potentials as compared to the ground state.[34]

Interestingly, the redox potentials of an excited state can be estimated thanks to the following expressions.

$$E^{*}\text{red} = E\text{red} + E_{0\text{–}0} \quad \text{Eq.10}$$

$$E^{*}\text{ox} = E\text{ox} - E_{0\text{–}0} \quad \text{Eq.11}$$

Eox and Ered are the redox potentials of the ground state while $E_{0\text{-}0}$ is the energy of the transition between the lowest-energy excited state and the ground state, each one being in its 0 vibrational level. Usually, $E_{0\text{-}0}$ is assimilated to the energy associated to the maximum emission wavelength of the given molecule. Based on the previous **equations 10** and **11**, the empirical Rehm-Weller relationship provides an estimate of the PET (photoinduced electron transfer) driving force.[34]

$$\Delta G_{PET} = E_{D/D+} - E_{A-/A} - E_{0\text{–}0} - e2/\varepsilon a \quad \text{Eq.12}$$

$E_{D/D+}$ and $E_{A\text{-}/A}$ represent respectively the oxidation potential of the donor and the reduction potential of the acceptor. $E_{0\text{-}0}$ is the energy of the transition 0-0 as mentioned before and the last term (e2/εa) describes the coulombic interaction between the two charged species which are formed by the reaction (e = elementary charge, ε = dielectric constant of the medium, a = distance between the species).[34]

Electron transfer quickly suggests electrochemistry, but the fields involved are much broader, touching on solid-state chemistry, biology (photosynthesis, cellular respiration, etc.), electron microscopy and more. Only transfers between metal centres and ligands were dealt with in the following, but this is only a small area of electron transfer.

6. Analyses of photophysical properties for future application

After having gone through the different ways of excitations and de-excitations, we are going to focus on what interests us: to take advantage of photon excitation to produce hydrogen. In this master thesis, we focused on the interactions between different photosensitizers and sacrificial electron donors to optimize the electron transfer to produce hydrogen.

The importance of the excited state lifetime must therefore be emphasized because it represents the experimental time window through which photo-induced electron transfer processes, which are of similar duration and therefore competitive with the intrinsic de-excitation, can be observed. It should therefore be checked whether an excited molecule M (in our case a metal complex) can interact with another molecule Q according to the scheme below (**Figure 14**) in which the k_q represents the rate constant observed for the bimolecular process.[29]

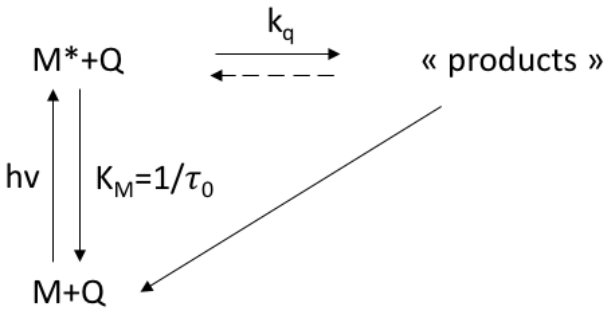

Figure 14-Differets pathways of a quenching reaction

To study the competition between these two processes (intermolecular reactivity and intrinsic deactivation of the excited state), we performed different analyses. This goal, i.e. to assess the reactivity of the excited state, can be probed by Stern-Volmer analysis.

7. Stern-Volmer

The Stern-Volmer equation, named after the physicists Otto Stern and Max Volmer, describes the kinetics of an intermolecular photochemical deactivation mechanism.

As shown above, examples of intramolecular deactivation mechanisms are fluorescence and phosphorescence. In contrast, intermolecular photo-induced deactivation is the action of a chemical species on accelerating the disappearance of another chemical species in the excited state. In general, this mechanism was represented by the **Figure 14**, where M and Q (called a "quencher") are chemical species, and * denotes an excited state. Emission spectroscopy, probing the gradual disappearance of the emission of A upon addition of increased concentration of quencher allows to monitor and quantify this quenching process. This experiment is called a “Stern-Volmer” analysis.

The kinetics of this mechanism obey the so-called Stern-Volmer equation:

$$\frac{I_f^0}{I_f} = 1 + k_q \tau_0 . [Q] \quad \text{Eq.13}$$

Where

- I_f^0 is the fluorescence intensity without any quencher
- I_f is the fluorescence intensity in presence of quencher
- k_q is the quenching rate constant
- τ_0 is the excited lifetime of A without quencher
- $[Q]$ is the quencher concentration

8. Marcus Theory

8.1 Why study the Marcus curve?

With the data obtained from the various analyses explained above, we might already have a good idea of how the different photosensitizer would behave, but it would be interesting to be able to exploit these data to determine kinetic constant for the induced photoelectron’s transfer. It helped us to select the best candidates for use in our final chain shown in the **Figure 6**. Indeed, as explained in the section, the aim is to be able to have a directional electron transfer from electron donor to the photosensitizer to efficiently regenerate the photocatalyst during the HER process. To achieve this, we need to optimize the driving force and the kinetic of this electron transfer event. Marcus' theory of electron transfer allows us to corelate the rate constant

of electron transfer (k_{ET}) to the standard free enthalpy of reaction (ΔG°).[37] This method explained below may therefore be interesting to analyse and assess the efficiency of the studied electron transfer event. But before going any further, it's worth taking a closer look at the theory itself.

8.2 Marcus theory

Marcus' theory has been developed by the Canadian scientist Rudolph Arthur Marcus and combines kinetic and thermodynamic parameters to predict the kinetic rate constants of electron transfer (k_{ET}) using different physical parameters. The most important among them are the driving force of the electron transfer (ΔG°), the reorganization energy before and after the electron transfer process) and the electronic coupling between the donor (D) and the acceptor (A) wave functions, H_{DA}.[37] His observations led to **equation 14** that can describe the behaviours of the complexes. A is a constant to simplify the original equation.

$$k_{et} = Ae^{\left(-\frac{(\Delta G^{\circ}+\lambda)^2}{4\lambda k_b T}\right)} \; A \sim 1 \times 10^{11}\; M^{-1}s^{-1} \quad \text{Eq. 14}$$

The reorganisation energy (λ) is the energy required for the distortion of a state (precursor) towards the equilibrium geometry of another state (successor). λ includes a part of energy of reorganization of the chemical bonds (λ_{in} inner sphere) and a reorganization of the solvent molecules (λ_{out} outer sphere). λ_{in} is often neglected because it is very small compared to λ_{out}.[37]

Electron transfer reactions involve the movement of an electron from a donor species to an acceptor species. During this process, the system undergoes a reorganization in its environment to accommodate the charge transfer. The reorganization energy represents the energy required for the surrounding medium to adjust and stabilize itself after the charge transfer occurs. It encompasses the changes in the structure and polarization of the solvent, including the rearrangement of solvent molecules, reorientation of dipoles, and relaxation of the surrounding electric field.

In Marcus theory, the overall rate of an electron transfer reaction is influenced by the reorganization energy. A higher reorganization energy leads to a slower reaction rate, as more energy is required to reorganize the environment. Conversely, a lower reorganization energy facilitates faster electron transfer.

The electronic coupling (H_{DA}) describes the stabilization energy gained from the interaction between the wave functions of the donor (D) and the acceptor (A).

The Marcus curve represents the relationship between the reaction rate (k_{ET}) and the driving force (ΔG) of an electron transfer reaction. The curve typically exhibits three distinct regions: the normal region, the saturation region, and the inverted region.

- Normal Region: The normal region of the Marcus curve is characterized by a positive slope, indicating that the reaction rate increases as the driving force increases. In this region, the reorganization energy (λ) is lower than the driving force. This region is often observed at smaller negative values of ΔG (second diagram in **Figure 15**).

- Barrierless Region: this region of the Marcus curve represents the region where the reaction rate plateaus and reaches its maximum value. In this region, the reorganization energy is equal the driving force (third diagram in **Figure 15**).

- Inverted Region: The inverted region of the Marcus curve refers to the region where the reaction rate decreases as the driving force increases. This occurs when the driving force get higher than the reorganization energy (λ). This recreates an activation barrier as shown in the **Figure 15**. The larger the driving force is compared to the reorganization energy, the higher the energy barrier will be, resulting in slower reaction rates. The inverted region is thus theoretically observed at large negative values of ΔG (last diagram in **Figure 15**).

It's important to note that the shape and position of the Marcus curve can be influenced by various factors, such as temperature, solvent properties, and the specific molecular systems involved. The curve thus provides insights into the relationship between reaction rates and driving forces in electron transfer processes, allowing for the analysis, and understanding of redox reactions in different environments.

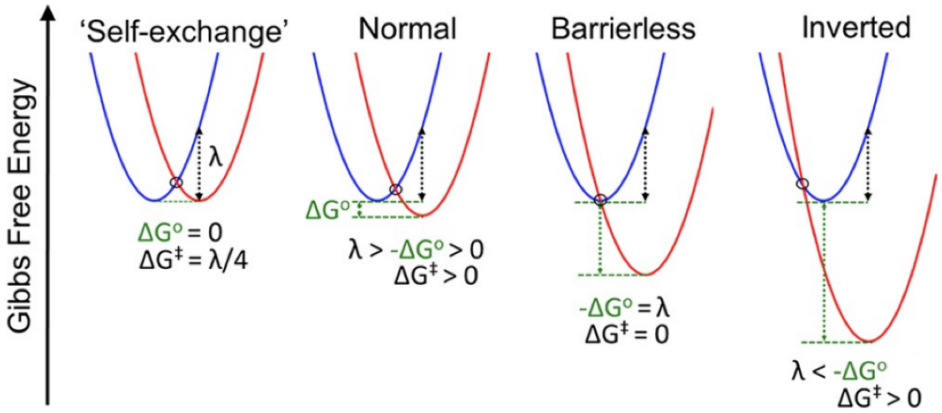

Figure 15-Evolution of the electron transfer kinetics as a function of the reorganization energy and the driving force [37]

8.3 Diffusion boundary problem

This introduction on Marcus' theory suggest that it is relatively simple to measure k_{et} and observe the inverse region, but this inverse region took a long time to be proven. It has even been controversial for a while by a part of the scientific world. It is only 28 years after the discovery of this equation by Marcus that it could really be proven. This earned him a Nobel Prize in 1992 "for his contribution to the theory of electron transfer reactions in chemical systems". The difficulty comes from the experimental measurement, which does not correspond to the speed constant of the single act of electron transfer, but of the overall process described in the **equation 15** below.

$$1 + 2 \leftrightarrows [1:2]^{\ddagger} \rightarrow [1^{+}:2^{-}] \rightarrow 1^{+} + 2^{-} \quad \text{Eq.15}$$

It is only in 1984 that Closs and Miller sought to overcome this limitation by using a rigid spacer between donor and acceptor (**Figure 16**).[38] They thus studied an intramolecular transfer so as not to be hindered by diffusion (k_a and k_{-a}). This enabled the inverse region to be observed for the first time. Indeed, by changing the nature of the donor and acceptor, they modified the value of ΔE° and obtained a curve with an inverted region.

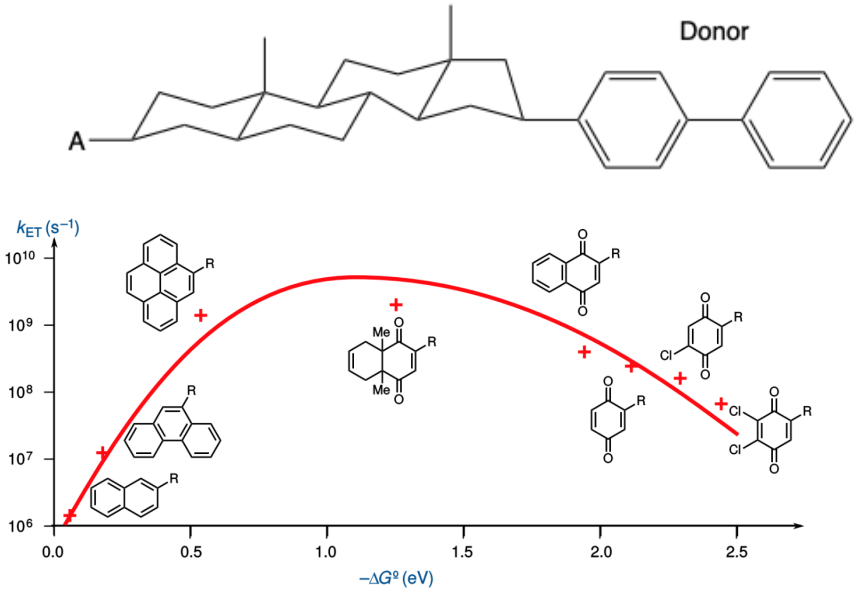

Figure 16-Marcus' curve observed by Closs and Miller [38]

II Objectives and Strategy

The overall objective of this master thesis is the synthesis and comprehensive photophysical and photochemical characterization of 9 mononuclear Ir(III) complexes $[Ir(piq)_2(LL)]^+.PF_6^-$ for electron transfer studies. The ultimate goal would be to use these compounds in photo-induced hydrogen molecular devices. To obtain these photosensitizers, we first synthesized (i) the precursor which is an iridium dimer $[Ir(piq)_2Cl]_2$. Once achieved, the dimers were coupled to 9 di-imine ligands (bipyridines and bipyrazine) in order to obtain these 9 photosensitizers (**Figure 17**). Several synthetic methods were tested and moderate to good yields for the synthesis were obtained.

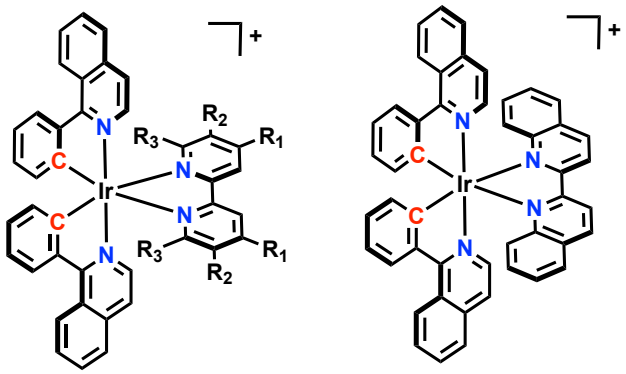

$[Ir(piq)_2(bpy)]^+$ (**1**): $R_1 = R_2 = R_3 = H$
$[Ir(piq)_2(4,4'\text{-}(CH_3)_2\text{-}bpy)]^+$ (**2**): $R_1 = CH_3$, $R_2 = R_3 = H$
$[Ir(piq)_2(5,5'\text{-}(CH_3)_2\text{-}bpy)]^+$ (**3**): $R_1 = H$, $R_2 = CH_3$, $R_3 = H$
$[Ir(piq)_2(6,6'\text{-}(CH_3)_2\text{-}bpy)]^+$ (**4**): $R_1 = R_2 = H$, $R_3 = CH_3$
$[Ir(piq)_2(4,4'\text{-}(^t Bu)_2\text{-}bpy)]^+$ (**5**): $R_1 = {}^t Bu$, $R_2 = R_3 = H$
$[Ir(piq)_2(4,4'\text{-}(C_9H_{19})_2\text{-}bpy)]^+$ (**6**): $R_1 = (CH_2)_8CH_3$ $R_2 = R_3 = H$
$[Ir(piq)_2(4,4'\text{-}(OCH_3)_2\text{-}bpyy)]^+$ (**7**): $R_1 = OCH_3$, $R_2 = R_3 = H$
$[Ir(piq)_2(4,4'\text{-}(Br)_2\text{-}bpy)]^+$ (**8**): $R_1 = Br$, $R_2 = R_3 = H$
$[Ir(piq)_2(biq)]^+$ (**9**): biq = 2,2'-biquinoline

Figure 17-The series of $[Ir(piq)_2(LL)]^+.PF_6^-$ photosensitizers investigated in the present work. [39]

To determine the feasibility of a quenching reaction of our photosensitizer, we characterized the photophysical and electrochemical properties of the different Ir(III) complexes. These results allowed us to investigate excited-state electron transfer with sacrificial electron donors that included triethanolamine (TEOA), triethylamine (TEA) and 1,3-dimethyl-2-phenyl-2,3-dihydro-1H-benzo[d]imidazole (BIH) in acetonitrile. The results presented hereafter were published in Photochemical & Photobiological Sciences by Springer.[39]

III Results and discussion

1 Synthesis

1.1 Synthesis of the iridium precursor

The synthetic approach to produce the series of iridium(III) photosensitizers relied on the use of iridium complexes with two cyclometalating piq ligands (piqH = 1-phenylisoquinoline). These ligands are relatively electron-rich, and cyclometalating ligands that are also known to increase the molar absorption coefficient of the resulting photosensitizers in the visible range[40]. The synthesis proceeded via the chelation of the cyclometalated ligands (providing an Ir(III) dichloro-bridged dimer), as described by Nonoyama[41] (**Figure 18**). To synthesize this dimer, we mixed $IrCl_3$.H2O and 1-phenylisoquinoline. We introduced more than twice the amount of the latest to ensure a good yield. The solvent of the reaction was 2-ethoxyethanol and water (ratio 3/1). The reaction mixture was heated to reflux under microwave (130°C, one hour, 200W) under inert atmosphere. After cooling to room temperature, addition of water led to the formation of a precipitate. This red powder is washed and filtered with water and then with diethyl ether and finally dried under vacuum.

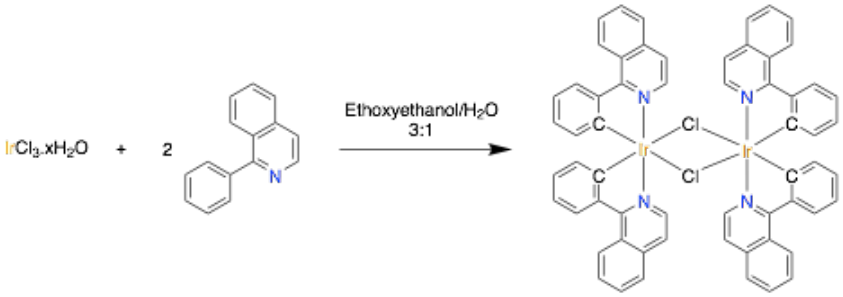

Figure 18-Synthetic scheme for the synthesis of Ir(III) dimers, precursors of the complexes.

Synthesis of Ligands

All the ligands were commercially available. It was thus not necessary to synthetize them for this master thesis.

1.2 Synthesis of [Ir(piq)$_2$(LL)]

After obtaining the dimers, the final complexes were obtained by the addition of N^N ligand. The N^N ligands were systematically varied over a wide range of ligand substitutions, which included 2,2'-bipyridine (bpy), 4,4'-, 5,5', and 6,6'-$(CH_3)_2$-2,2'-bipyridine, 4,4'-$(OCH_3)_2$-2,2'-bipyridine, 4,4'-(^{t}Bu)$_2$-2,2'-bipyridine, 4,4'-$(C_9H_{19})_2$-2,2'-bipyridine, 4,4'-$(Br)_2$-2,2'-bipyridine as well as 2,2'-biquinoline (biq). The modifications of the N^N diimine ligands influenced the LUMO energy level of each complex, which in turn altered the visible light absorption properties, as well as the ground-state and excited-state reduction potentials, $E_{1/2}(Ir^{+*/0})$. To add the N^N ligands to the Iridium dimer, we used two different methods.

The first method of synthesis consisted in the addition of Ir(III) chloro-bridged dimer [Ir(piq)$_2$μ-Cl]$_2$ and the N^N ligand in an ethylene glycol solution in a microwave tube (**Figure 19.1**). The reaction mixture was heated in an inert atmosphere (argon) at 200W (microwave), 130°C for one hour. After reaction, the orange-red mixture was cooled down to room temperature. The resulting solution was treated with different volumes of milliQ water and an excess of NH_4PF_6 was then added. The complex was isolated by centrifugation and was washed 3 times with milliQ water and 3 times with diethyl ether to give the desired complexes with yields that ranged from 36 to 67 %. This first method was relatively effective, but there were problems with purity. There were many traces of precursors at the end of the synthesis. This necessitated the use of column purification, which led to losses in the final yield. We therefore tested a new synthesis method to obtain a better yield and at the same time reduce the synthesis time by reducing the post-production processing time.

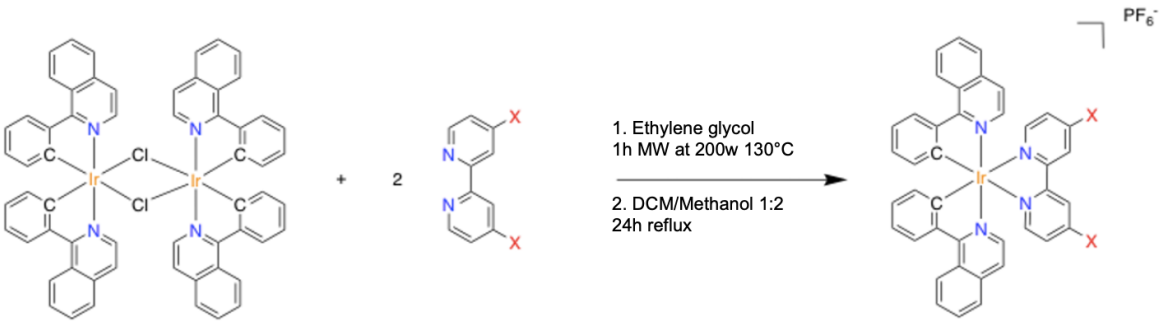

Figure 19-Synthetic scheme for the synthesis of [Ir(piq)$_2$(LL)]

For the second method of synthesis, it consisted in placing the Ir(III) chloro-bridged dimer $[Ir(piq)_2\mu\text{-}Cl]_2$ and the corresponding diimine ligand in a sealed tube under argon atmosphere in a solution of methanol and dichloromethane mixture (**Figure 19.2**). The reaction was heated at 60 °C for 24 hours. After reaction, the orange-red mixture was cooled down to room temperature. The DCM fraction was evaporated, and the resulting solution was treated with different volumes of milliQ water and an excess of NH_4PF_6 was then added. The complex was isolated by centrifugation and was washed 3 times with milliQ water and 3 times with diethyl ether to give the desired complexes with yields that ranged from 57 to 82 %.

This second method of synthesis allowed for better yields and cleaner products. Indeed, we have on average a yield of 50% for the first method and an average yield of 71% for the second. To ensure good purity of the compounds, we proceeded to an NMR analysis of all the products obtained.

2 Photophysics

In order to understand the behaviour of the molecules, it is important to study the physical properties of the complexes, and thus their absorption and emission of light. To do so, we made different analysis described below. All the data of photophysical properties of photosensitizers 1-9 are listed in **Table 1**.

Table 1. Photophysical properties of photosensitizers 1-9 recorded in acetonitrile

Compound	Abs (ε)	L_{max}	τ (ns)	φ[a]	k_r (x$10^4 s^{-1}$)	k_{nr} (x$10^6 s^{-1}$)
$[Ir(piq)_2(bpy)]^+$ (1)	438 (6300)	30, 594	2580	0.108 (0.024)	4.84	0.34
$[Ir(piq)_2(4,4'\text{-}(CH_3)_2\text{-}bpy)]^+$ (2)	440 (6500)	31, 593	3210	0.143(0.025)	4.76	0.26
$[Ir(piq)_2(5,5'\text{-}(CH_3)_2\text{-}bpy)]^+$ (3)	440 (6000)	29, 594	3160	0.151(0.024)	4.83	0.27
$[Ir(piq)_2(6,6'\text{-}(CH_3)_2\text{-}bpy)]^+$ (4)	434 (6000)	37, 601	3350	0.143(0.027)	4.20	0.26
$[Ir(piq)_2(4,4'\text{-}(^tBu)_2\text{-}bpy)]^+$ (5)	441 (5900)	30, 594	1410	0.145 (0.022)	10.6	0.60
$[Ir(piq)_2(4,4'\text{-}(C_9H_{19})_2\text{-}bpy)]^+$ (6)	441 (6200)	30, 592	3180	0.137 (0.053)	4.31	0.27
$[Ir(piq)_2(4,4'\text{-}(OCH_3)_2\text{-}bpy)]^+$ (7)	442 (5900)	30, 596	2960	0.161 (0.030)	5.52	0.28
$Ir(piq)_2(4,4'\text{-}(Br)_2\text{-}bpy)]^+$ (8)	436 (5400)	35	250	0.029 (0.020)	12.1	3.88
$[Ir(piq)_2(biq)]^+$ (9)	427 (7900)	69	313	0.063 (0.044)	20.4	2.99

[a]Values for air-equilibrated solution in parenthesis

2.1 Absorption spectroscopy

The photophysical behaviour of the different Ir(III) based photosensitizers have been first studied by absorption spectroscopy (**Figure 20**). As explained in the introduction part, this analysis is interesting to understand the complexes photophysical properties. The UV-visible absorption features of all complexes were characterized by strong ligand-centred (LC) absorption bands in the UV region (**Figure 20**). The transitions observed at wavelengths greater than 350 nm are often assigned to mixed metal-to-ligand (MLCT) and ligand-to-ligand (LLCT) charge transfer bands as well as metal-ligand-to-ligand charge transfer (MLLCT) from the cyclometalating ligand to the N^N ligand[40,42,43]. These transitions were determined to have molar absorption coefficients in the 5400-7900 $M^{-1}cm^{-1}$ range at 427-442 nm (**Table 1**).

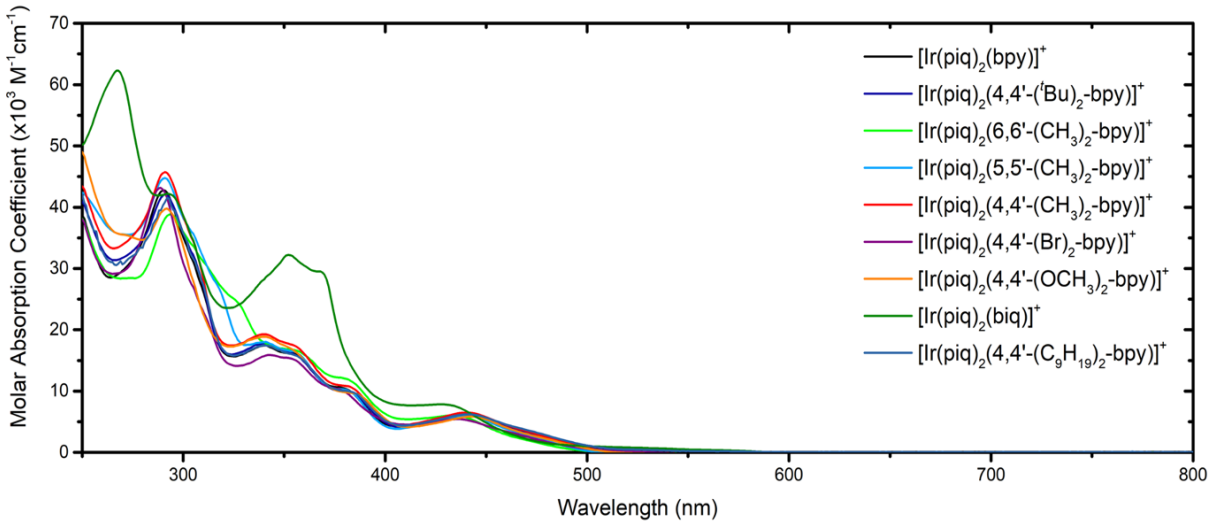

Figure 20-UV-visible absorption spectra Ir(piq)2(bpy)]+ (black), [Ir(piq)2(4,4'-(tBu)2-bpy)]+ (blue), [Ir(piq)2(6,6'-(CH3)2-bpy)]+ (green), [Ir(piq)2(5,5'-(CH3)2-bpy)]+ (light blue), [Ir(piq)2(4,4'-(CH3)2-bpy)]+ (red), [Ir(piq)2(4,4'-(Br)2-bpy)]+ (purple), [Ir(piq)2(4,4'-(OCH3)2-bpy)]+ (orange), [Ir(piq)2(biq)]+ (olive) and [Ir(piq)2(4,4'-(C9H19)2-bpy)]+ (pale blue) recorded in acetonitrile at room temperature under argon

On the **Figure 20**, all the $[Ir(piq)_2(bpy)]^+$ display very similar absorption spectra. Only the $[Ir(piq)_2(biq)]^+$ has a spectrum presenting slightly hypsochromic shift compared to the other Ir(III) complexes. As shown in the introduction, ligands can influence the electronic structure and energy levels. Ligand field effects arise from the interaction between the metal ion and the ligands, leading to changes in the electronic transitions and spectral properties. As we only modify N^N ligand, only LUMO energy is modified. In the case of biquinoline, LUMO is destabilized with electron-donating groups as biquinoline can act as a π-conjugated system with

delocalized π-electrons. The destabilisation of the LUMO enhance the gap between HOMO-LUMO and thus the absorption will occur in a higher energy.

2.2 Emission spectroscopy and excited state lifetime

After the analysis of the absorption of the compounds, we wanted to analyse their emissions (**Figure 21**). The emission wavelength is related to the energy difference between the excited state and the ground state of the complex (HOMO-LUMO gap). If the energy gap between these states is larger, the emitted light will have a longer wavelength. Thus, the same reasoning applies as to absorption, the LUMO will be destabilized with electron-donating groups of biquinoline, which will increase the HOMO-LUMO gap and therefore, as seen in the **Figure 21**, the emission spectrum of complex 9 (dark green) are shifted bathochromically.

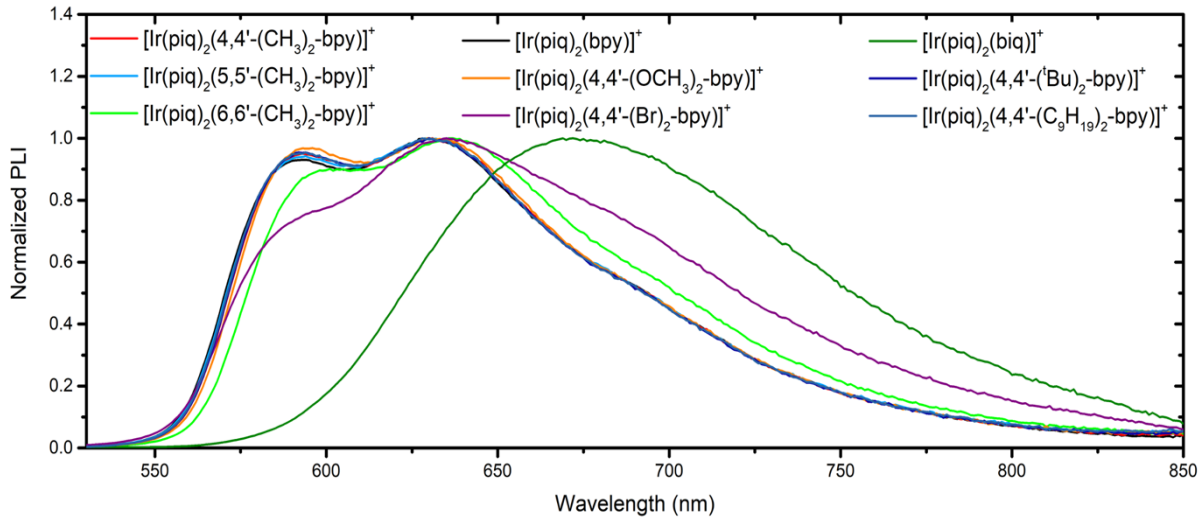

Figure 21 -UV-visible emission spectra Ir(piq)2(bpy)]+ (black), [Ir(piq)2(4,4'-(tBu)2-bpy)]+ (blue), [Ir(piq)2(6,6'-(CH3)2-bpy)]+ (green), [Ir(piq)2(5,5'-(CH3)2-bpy)]+ (light blue), [Ir(piq)2(4,4'-(CH3)2-bpy)]+ (red), [Ir(piq)2(4,4'-(Br)2-bpy)]+ (purple), [Ir(piq)2(4,4'-(OCH3)2-bpy)]+ (orange), [Ir(piq)2(biq)]+ (olive) and [Ir(piq)2(4,4'-(C9H19)2-bpy)]+ (pale blue) recorded in acetonitrile at room temperature under argon

The complexes were excited in the visible blue light range (440 nm). Blue light excitation yielded photoluminescence (PL) decays that were in all cases well described using a bi-exponential decay. Irrespective of the nature of the photosensitizer, a short excited-state lifetime (15 ± 2 ns) was measured in all cases, which probably arose from a piq-centered deactivation. The second component of the excited-state lifetime, tabulated in **Table 1**, was strongly influenced by the nature of the N^N ligand, where electron withdrawing groups such

as in 4,4'-$(Br)_2$-2,2'-bipyridine and 2,2'-biquinoline exhibited shorter excited-state lifetimes (τ) of 250 and 313 ns, respectively, while photosensitizers bearing more electron-rich ligands exhibited lifetimes values between 1.41 µs and 3.35 µs, (**Table 1**).

2.3 Quantum yields

The photoluminescence quantum yields (ϕ_{PL}), under air and in argon-purged solutions, were determined by comparative actinometry (**equation 16**) using $[Ru(bpy)_3]^{2+}$ as the actinometer (act)[44]. In **equation 16**, PL refers to the integrated photoluminescence spectra, A to the absorbance of the solution at the excitation wavelength, and η to the refractive index of the solvent. $[Ir(piq)_2(4,4'\text{-}(Br)_2\text{-}bpy)]^+$ and $[Ir(piq)_2(biq)]^+$ each exhibited a moderate ϕ_{PL} of 0.029 and 0.063 under argon, respectively (**Table 1**). All other photosensitizers exhibited a ϕ_{PL} between 0.108 and 0.161 under argon. Interestingly, for the photosensitizers with τ greater than 1 µs, ϕ_{PL} was always 4 to 6 times greater under argon than under air, indicating the possibility of $^1O_2$ photosensitization.

$$\phi_{PL}^{PS} = (\phi_{PL}^{Act})\left(\frac{PL^{PS}}{PL^{Act}}\right)\left(\frac{1-10^{-A^{Act}}}{1-10^{-A^{PS}}}\right)\left(\frac{\eta_{PS}^2}{\eta_{Ru}^2}\right) \quad \text{Eq. 16}$$

2.4 Excited state lifetime

It consists in the excitation of a compound A via a small quantum of photon (flash) and then we measure the decrease of the excited complex A* luminescence intensity. This decrease follows an exponential trend described in **equation 17**. Integrating this equation over the time gives the **equation 18**.

$$\frac{-d[A^*]}{dt} = (k_r + k_{nr})[A^*] \quad \text{Eq. 17}$$

$$[A^*](t) = [A^*](0)e[-(k_r + k_{nr})t] = [A^*](0)e\left(\frac{t}{\tau}\right) \quad \text{Eq. 18}$$

At any time t, the concentration of an excited state A* can thus be determined from its initial concentration and its lifetime. Electron transfer from the excited state of the photosensitizer to the acceptors is a fundamental step in the TCS (three-component system). Comparing the excited state lifetimes helps in optimizing the electron transfer efficiency in complex systems. Complexes with longer excited state lifetimes may indicate more favourable energy level alignment and reduced non-radiative decay pathways, in turn leading to improved electron transfer efficiency. By identifying complexes with longer excited state lifetimes, researchers can focus on enhancing their stability, reducing relaxation losses, and optimizing the conditions for efficient electron transfer.

Between all the synthetized complexes, only two have an excited lifetime below 500 ns. Indeed $Ir(piq)_2(4,4'\text{-}(Br)_2\text{-}bpy)]^+$ and $[Ir(piq)_2(biq)]^+$ have an excited lifetime of respectively 250 and 313 which is, compared to the other complexes, short.

3 Electrochemistry

3.1 Differential pulse and cyclic voltammetry

Cyclic voltammetry and pulse voltammetry (**Figure 22**) were used to determine the oxidation and reduction potential of the reference complexes in their fundamental state. These potentials were measured in CH_3CN under inert atmosphere. The nine photosensitizers exhibited reversible $Ir^{IV/III}$ reduction waves at potentials centred between 1.21 and 1.33 V vs NHE. The introduction of electron-withdrawing derivatives, such as $4,4'\text{-}(Br)_2$-2,2'-bipyridine and 2,2'-biquinoline had little influence on the $Ir^{IV/III}$ redox couple. On the other hand, the ligand-centred reductions were strongly influenced by the nature of the substituents on the 2,2'-bipyridine backbone. Compared to $[Ir(piq)_2(bpy)]^+$, which displayed a first one-electron ligand-centred reduction at –1.35 V vs NHE, derivatives with electron donating substituents in the 4,4', 5,5' or 6,6' position shifted the reduction potentials 60-120 mV more negative. The introduction of $4,4'\text{-}(C_9H_{19})_2$-2,2'-bipyridine resulted in a 10 mV anodic shift compared to the prototypical $[Ir(piq)_2(bpy)]^+$. The most drastic shifts were observed for the photosensitizers bearing $4,4'\text{-}(Br)_2$-2,2'-bipyridine and 2,2'-biquinoline ligands, where the ligand-centred reductions were shifted by +320 mV and +410 mV, respectively. The corresponding excited state reduction (E_{red}*) and oxidation (E_{ox}*) potentials were determined using **equations 19** and **20**, where E_{00} is corresponds to the free energy stored in the excited state.[45,46] As expected

based on ground-state reduction potentials, $[Ir(piq)_2(4,4'\text{-}(Br)_2\text{-}bpy)]^+$ and $[Ir(piq)_2(biq)]^+$ were the most potent photo-oxidants, with E_{red}* of 1.41 and 1.37 V vs NHE, respectively. The other 7 photosensitizers had very similar E_{red}* (**Table 2**).

$$E_{red}* = E_{1/2}\,(Ir^{*(0/-)}) = E_{1/2}(L^{n/n-1}) + E_{00} \qquad \text{Eq. 19}$$

$$E_{ox}* = E_{1/2}\,(Ir^{*(+/0)}) = E_{1/2}(Ir^{IV/III}) - E_{00} \qquad \text{Eq. 20}$$

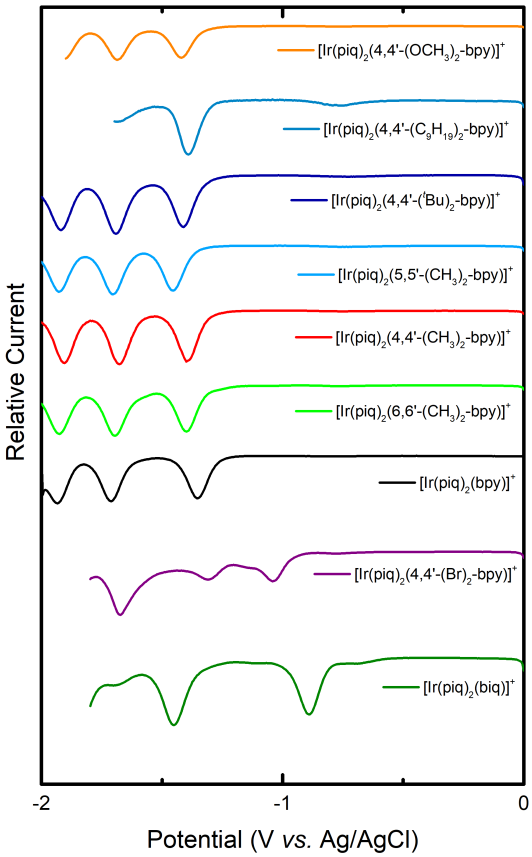

Figure 22. *Differential pulse voltammetry of $[Ir(piq)_2(bpy)]^+$ (black), $[Ir(piq)_2(4,4'\text{-}(^tBu)_2\text{-}bpy)]^+$ (blue), $[Ir(piq)_2(6,6'\text{-}(CH_3)_2\text{-}bpy)]^+$ (green), $[Ir(piq)_2(5,5'\text{-}(CH_3)_2\text{-}bpy)]^+$ (light blue), $[Ir(piq)_2(4,4'\text{-}(CH_3)_2\text{-}bpy)]^+$ (red), $[Ir(piq)_2(4,4'\text{-}(Br)_2\text{-}bpy)]^+$ (purple), $[Ir(piq)_2(4,4'\text{-}(OCH_3)_2\text{-}bpy)]^+$ (orange), $[Ir(piq)_2(biq)]^+$ (olive) and $[Ir(piq)_2(4,4'\text{-}(C_9H_{19})_2\text{-}bpy)]^+$ (pale blue) recorded in 0.1M $TBAPF_6$ acetonitrile electrolyte at room temperature.*

[a]The E_{oo} was determined using the generalizable method of extrapolating a tangent line on the blue edge of the corrected PL spectrum to the emission baseline.

Table 2. Ground and excited-state reduction potentials for photosensitizers 1-11

Complex	$E_{1/2}(Ir^{IV/III})$ V vs NHE	$E_{1/2}(L^{n/n-1})$ V vs NHE	E_{00} (eV)[a]	Eox* V vs NHE	*Ered** V vs NHE
$[Ir(piq)_2(bpy)]^+$ (1)	1.28	–1.35	2.23	–0.75	1.08
$[Ir(piq)_2(4,4'\text{-}(CH_3)_2\text{-}bpy)]^+$ (2)	1.25	–1.43	2.23	–0.78	0.99
$[Ir(piq)_2(5,5'\text{-}(CH_3)_2\text{-}bpy)]^+$ (3)	1.28	–1.47	2.23	–0.75	0.96
$[Ir(piq)_2(6,6'\text{-}(CH_3)_2\text{-}bpy)]^+$ (4)	1.25	–1.42	2.21	–0.77	0.99
$[Ir(piq)_2(4,4'\text{-}(^tBu)_2\text{-}bpy)]^+$ (5)	1.26	–1.41	2.23	–0.77	1.02
$[Ir(piq)_2(4,4'\text{-}(C_9H_{19})_2\text{-}bpy)]^+$ (6)	1.27	–1.34	2.23	–0.76	1.01
$[Ir(piq)_2(4,4'\text{-}(OCH_3)_2\text{-}bpy)]^+$ (7)	1.24	–1.46	2.22	0.78	0.96
$[Ir(piq)_2(4,4'\text{-}(Br)_2\text{-}bpy)]^+$ (8)	1.33	–1.03	2.24	–0.71	1.41
$[Ir(piq)_2(biq)]^+$ (9)	1.21	–0.94	2.11	–0.70	1.37

[a]The E_{oo} was determined using the generalizable method of extrapolating a tangent line on the blue edge of the corrected PL spectrum to the emission baseline. [47,48]

3.2 Stern Volmer

In this section, two additional complexes are studied: $Ir(piq)_2$ complexes with 4,4'-$(CF_3)_2$-bpy (called 10) and bipyrazine (called 11) as N^N ligands are added. The interest in these two are their electron-withdrawing effects. This electron withdrawal can affect the energy levels and electronic transitions, leading to a higher energy gap between the excited and ground states. As a result, the complex may exhibit reliable emission at longer wavelengths, placing it in the inverse region of Marcus theory.

These are synthetized and obtained in the same way as the other 9 complexes. The results obtained for the 11 complexes are shown in the **Table 3**. However, these two complexes have generated uncertainty in determining the rate constant (k_q) due to reliable emission and low excited state lifetimes, and this is why they were not present in the first series of 9.

Excited-state reactivity of all $[Ir(piq)_2(LL)]^+$ photosensitizers towards TEA, TEOA and BIH as sacrificial electron donors was investigated in argon-purged acetonitrile using the Stern-Volmer analysis (see introduction). The driving force for electron transfer with BIH, TEOA and TEA was estimated based on available ground and excited-state reduction potentials.

With BIH as sacrificial electron donor, the driving force for electron transfer from all complexes was exergonic, with the Gibbs free energy for electron transfer, ΔG, ranging from –0.39 V for $[Ir(piq)_2(4,4'\text{-}(OCH_3)_2\text{-}bpy)]^+$ to –0.83 V with $[Ir(piq)_2(4,4'\text{-}(Br)_2\text{-}bpy)]^+$.

With TEA and TEOA as the electron donors, ΔG was almost always ergoneutral or slightly endergonic. From the tabulated values in **Table 3**, ΔG became more exergonic with more potent photo-oxidants, *i.e.* $[Ir(piq)_2(4,4'\text{-}(Br)_2\text{-}bpy)]^+$ and $[Ir(piq)_2(biq)]^+$. This observation in driving force was also evident from Stern-Volmer measurements (**Figure 18**). A representative result of a Stern-Volmer titration using $[Ir(piq)_2(6,6'\text{-}(CH_3)_2\text{-}bpy)]^+$ with BIH, TEA and TEOA as the electron donors is shown in **Figure 23**.

With BIH, drastic quenching of the steady-state photoluminescence was observed. The corresponding Stern-Volmer plot was linear within the quencher concentration range examined and, from the slope, a quenching rate constant (k_q) of 5.3 x10^9 $M^{-}1s^{-1}$ was determined.

With TEA and TEOA, only moderate excited-state quenching was observed and the corresponding Stern-Volmer plots exhibited a downward curvature. This downward curvature was observed for almost all the iridium(III) photosensitizers investigated in this study. Although a corresponding quenching rate constant could not be unambiguously determined, **Figure 18d** indicates that the excited-state quenching was approximately three orders of magnitude smaller (10^6 $M^{-1}s^{-1}$) than with BIH. The Stern-Volmer plots for the excited-state quenching of the nine Ir(III) photosensitizers with BIH are shown in **Figure 23e**. The Stern-Volmer plots were all linear and the corresponding quenching rate constants were determined in the range of 1.6x10^9 $M^{-1}s^{-1}$ to 7.1x10^9 $M^{-1}s^{-1}$ (**Table 3**). A rather counterintuitive quenching behaviour was noted for photosensitizers $[Ir(piq)_2(4,4'\text{-}(Br)_2\text{-}bpy)]^+$ and $[Ir(piq)_2(biq)]^+$ where a smaller k_q was obtained despite having larger ΔG for electron transfer compared to other photosensitizers in the series studied.

Instead, it was found that the decrease in k_q could likely result from reduced stability of both complexes upon illumination. Indeed, with $[Ir(piq)_2(4,4'\text{-}(Br)_2\text{-}bpy)]^+$ it was observed that allowing lighter to excite the photosensitizer, by using wider excitation slits, resulted in some degradation that was detected as an increase in photoluminescence upon titration with BIH (see later photostability experiments). To observe genuine quenching, the opening of the excitation slit had to be kept minimal. With $[Ir(piq)_2(biq)]^+$, degradation was not observed with BIH, but with TEA as a quencher, a novel, more energetic photoluminescent band appeared (**Figure S16**). Such an observation has already been recorded with $[Ir(ppy)_2(4,4'\text{-}(^t\text{Bu})_2\text{-}bpy)]^+$ and $[Ir(ppy)_2(bpy)]^+$ and is more in line with an irreversible reduction of the N^N ligand.[49,50] Hence, we hypothesized that neither $[Ir(piq)_2(4,4'\text{-}(Br)_2\text{-}bpy)]^+$ nor $[Ir(piq)_2(biq)]^+$ would exhibit

reversible behaviour upon steady-state illumination and/or photoreduction catalysis, but that the other seven photosensitizers would be attractive candidates.

Table 3. Driving force (ΔG) and quenching rate constants (kq) for electron transfer between BIH, TEOA or TEA and excited photosensitizers 1-9.a

Compound	ΔG_{BIH} (eV)	ΔG_{TEOA} (eV)	ΔG_{TEA} (eV)	k_q (BIH) ($M^{-1}s^{-1}$)
[Ir(piq)$_2$(bpy)]$^+$ (1)	–0.51	0.00	–0.06	7.1 x10^9
[Ir(piq)$_2$(4,4'-(CH$_3$)$_2$-bpy)]$^+$ (2)	–0.42	0.09	0.03	3.7 x10^9
[Ir(piq)$_2$(5,5'-(CH$_3$)$_2$-bpy)]$^+$ (3)	–0.39	0.12	0.06	3.8 x10^9
[Ir(piq)$_2$(6,6'-(CH$_3$)$_2$-bpy)]$^+$ (4)	–0.42	0.09	0.03	5.3 x10^9
[Ir(piq)$_2$(4,4'-(^{t}Bu)$_2$-bpy)]$^+$ (5)	–0.44	0.06	0.00	5.1 x10^9
[Ir(piq)$_2$(4,4'-(C$_9$H$_{19}$)$_2$-bpy)]$^+$ (6)	–0.44	0.07	0.01	2.4 x10^9
[Ir(piq)$_2$(4,4'-(OCH$_3$)$_2$-bpy)]$^+$ (7)	–0.39	0.12	0.06	2.9 x10^9
[Ir(piq)$_2$(4,4'-(Br)$_2$-bpy)]$^+$ (8)	–0.83	–0.33	–0.39	1.9 x10^9
[Ir(piq)$_2$(biq)]$^+$ (9)	–0.79	–0.29	–0.35	1.6 x10^9
[Ir(piq)$_2$(4,4'-(CF$_3$)$_2$-bpy)]$^+$ (10)	–0.81	–0.30	–0.36	3.7 x10^8
[Ir(piq)$_2$(bpz)]$^+$ (11)	–1.01	–0.51	–0.57	1.7 x10^9

[a] k_q with TEA and TEOA were in the 10^6 $M^{-1}s^{-1}$ range

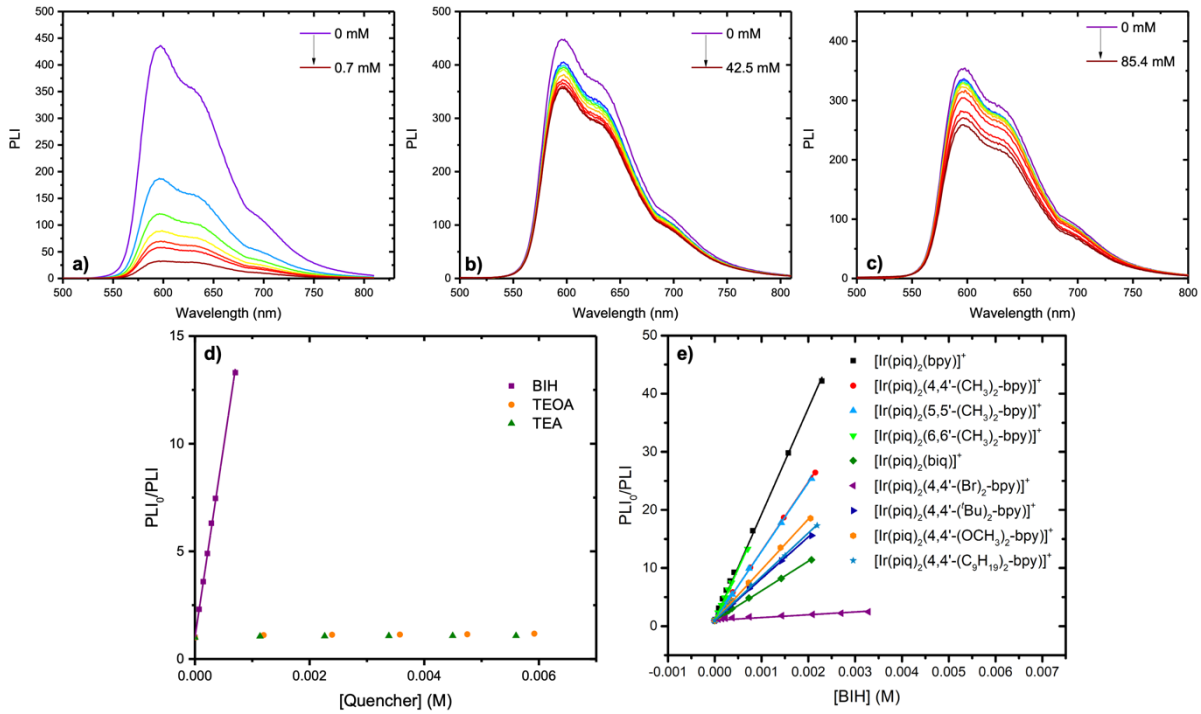

Figure 23. *Excited-state quenching of [Ir(piq)$_2$(6,6'-(CH$_3$)$_2$-bpy)]$^+$ with BIH (a), TEOA (b) and TEA (c) in argon purged acetonitrile. The corresponding Stern-Volmer plots is shown in panel d, with the corresponding linear fit for the excited-state quenching in the presence of BIH. The Stern-Volmer plots and corresponding linear fit for the excited-state quenching of all Ir(III) photosensitizers in the presence of BIH is shown in panel e.*

3.3 Reversibility after accumulation of the mono-reduced photosensitizer

Finally, a steady-state illumination was performed to investigate the possibility of reversible accumulation of the mono-reduced photosensitizers. Consequently, solutions of the iridium(III) photosensitizers with an absorbance around 0.5 in the visible region were prepared in argon-purged acetonitrile. BIH was added to reach a concentration of 1 mM. The solutions were then irradiated with commercial blue LED strips for 15 minutes and absorption spectra were recorded at specific time intervals. **Figure 24** shows representative data for $[Ir(piq)_2(bpy)]^+$, $[Ir(piq)_2(4,4'\text{-}(CH_3)_2\text{-}bpy)]^+$, $[Ir(piq)_2(biq)]^+$ and $[Ir(piq)_2(4,4'\text{-}(Br)_2\text{-}bpy)]^+$. Steady-state illuminations with the other photosensitizers are gathered in the supporting information (**Figures S18-S22**). With $[Ir(piq)_2(bpy)]^+$ and $[Ir(piq)_2(4,4'\text{-}(CH_3)_2\text{-}bpy)]^+$, blue light excitation led to changes in absorbance that agreed with excited-state electron transfer from BIH to the excited photosensitizers and subsequent mono-reduced complex formation. Indeed, the double absorption peaks at 500 and 530 nm, coupled with the increased absorbance beyond 700 nm were in line with absorption changes observed in transient absorption spectroscopy with related photosensitizers.

After 15 minutes of irradiation, an excess of potassium persulfate ($K_2S_2O_8$) was added as an irreversible electron acceptor to oxidize the monoreduced Ir photosensitizer and recover the ground-state Ir^{III} products. $[Ir(piq)_2(bpy)]^+$ and $[Ir(piq)_2(4,4'\text{-}(CH_3)_2\text{-}bpy)]^+$ showed full reversibility upon the addition of $K_2S_2O_8$, highlighting their great photostability when storing high energy electrons and hence their promise as efficient photosensitizers for applications in reductive catalysis. When $[Ir(piq)_2(4,4'\text{-}(Br)_2\text{-}bpy)]^+$ was used, an increase of the absorbance around 400 nm was rapidly observed with irradiation. Upon addition of $K_2S_2O_8$, this absorption band decreased, but the original spectrum was never recovered, suggesting the instability of this photosensitizer upon prolonged illumination in the presence of electron donors. Finally, $[Ir(piq)_2(biq)]^+$ was also irradiated in the presence of BIH and showed the irreversibility of the photoreduction event (**Figure 24-c**).

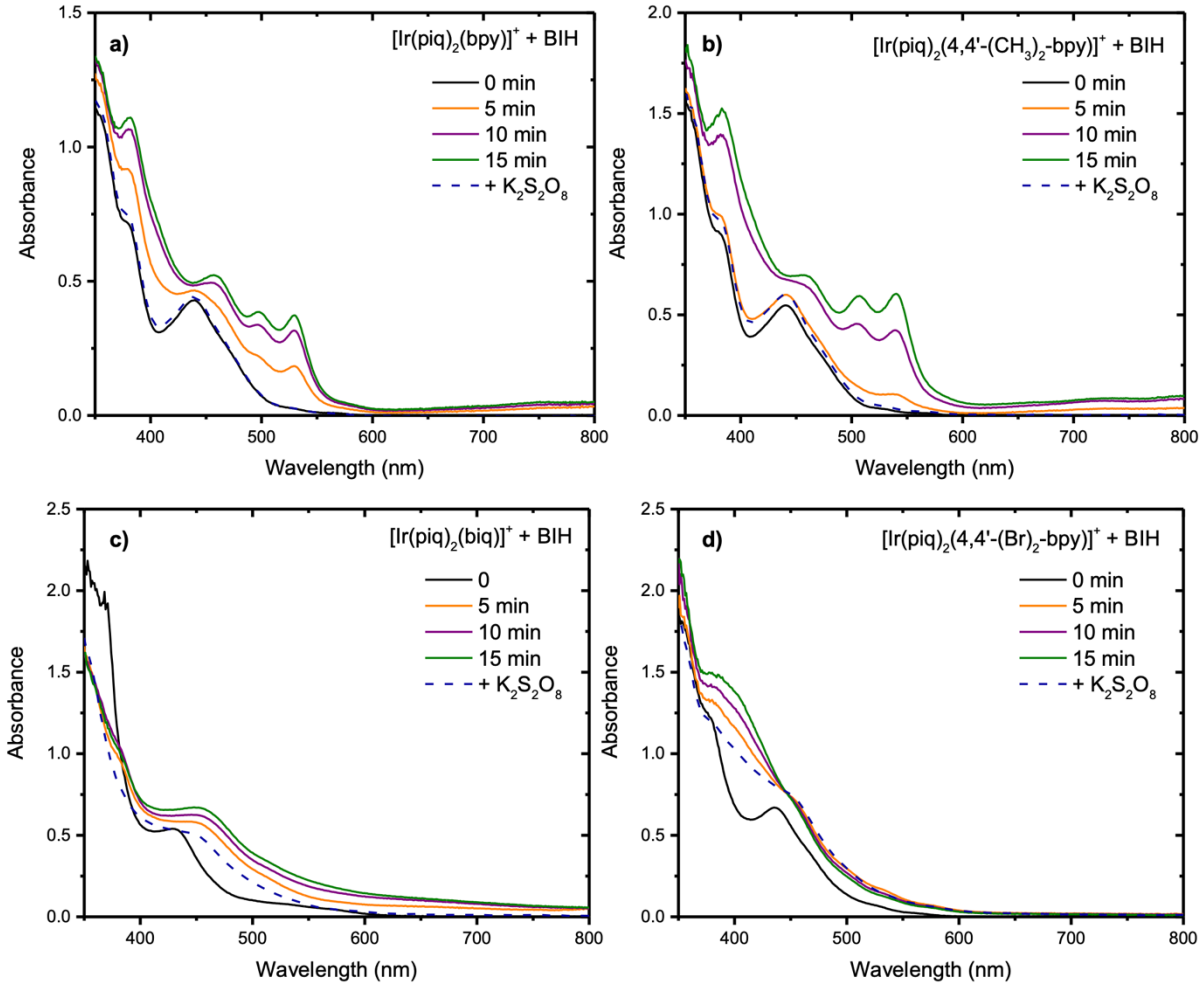

Figure 24. *Absorption spectra of $[Ir(piq)_2(bpy)]^+$ (a), $[Ir(piq)_2(4,4'\text{-}(CH_3)_2\text{-}bpy)]^+$ (b), $[Ir(piq)_2(biq)]^+$ (c) and $[Ir(piq)_2(4,4'\text{-}(Br)_2\text{-}bpy)]^+$ (d) in argon-purged acetonitrile at room temperature at t= 0 minutes (black) and following 5 minutes (orange), 10 minutes (purple) and 15 minutes (olive) irradiation with blue LED light in the presence of 1 mM BIH. After the irradiation, an excess of $K_2S_2O_8$ was added to oxidize the photo-reduced photosensitizer and investigate reversibility.*

3.4 Marcus Curve: Link between thermodynamic and kinetic

In this part, we analysed the link between thermodynamic and kinetic with Marcus' theory. We could obtain the data with the analysis made with stern-Volmer and cyclic voltammetry. As described above, with stern-Volmer measurements we could obtain the kinetic quenching rate constants (k_q) and we could calculate de ΔG with the analysis of the cyclic voltammetry results (**equation 12**).

The plot of k_q vs ΔG is shown in **Figure 25**. Strikingly, a decrease of the rate of electron transfer is clearly shown upon increased exergonicity of the electron transfer. Although

preliminary and uncommon, this result highlights the possibility of observing the Marcus inverted region.[51,52,53,54] At the peak of the Marcus curve, the rate constant corresponds to the transition state, where the electron transfer reaction occurs with the highest probability. After observing **Figure 25**, we could therefore determine that the $[Ir(piq)_2(bpy)]^+$ is the complex in our series that would be the most effective photosensitizer in our system presented in the introduction **Figure 6** for an electron transfer to the catalytic centre.

It should be stressed that those quenching rate constant were determined by steady-state photoluminescence quenching and the experiments with compound 10 and compound 11 were the most challenging to perform due to the very low photoluminescence quantum yield. Hence, these two date points are the one with the larger error, yet they are the most important one as they are in the Marcus inverted region and show the decrease in quenching rate constant as the driving force is increased. Hence, careful analysis and further investigation, notably by time-resolved photoluminescence and transient absorption spectroscopy are required and necessary to unambiguously determine if the Marcus inverted region is present in this case. Careful analysis and further investigation are necessary to differentiate between the effects of Marcus' curve and diffusion limitations in the system under study.

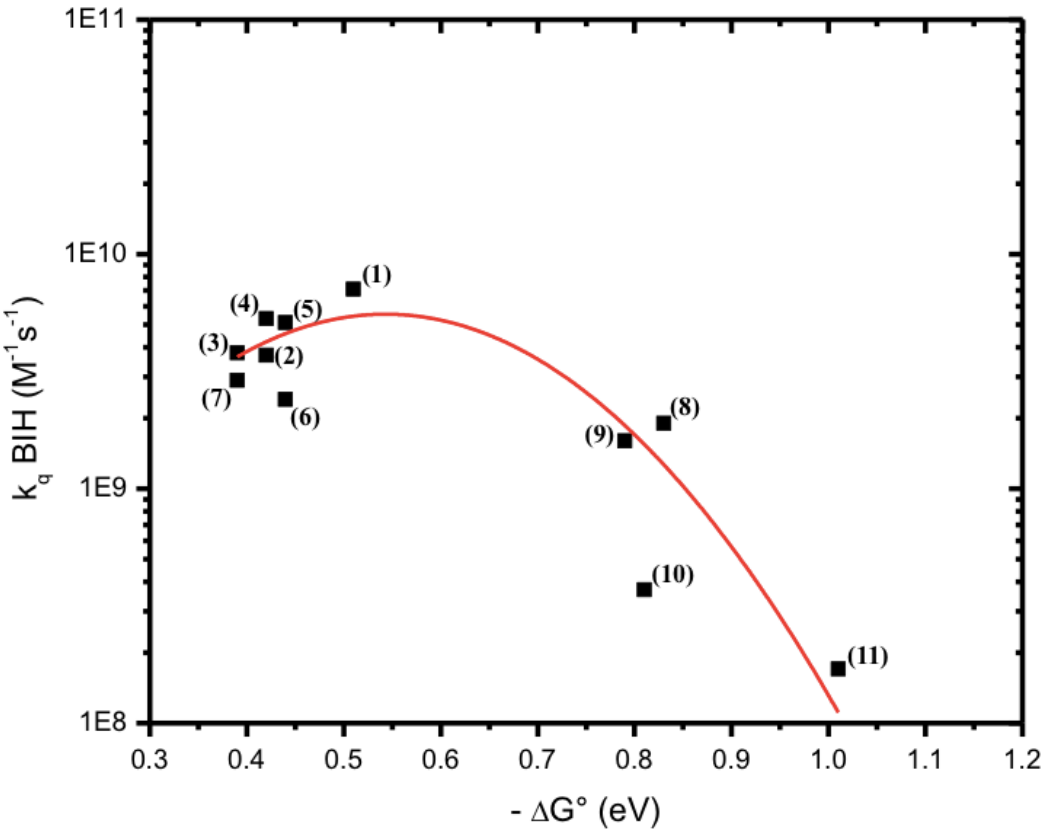

Figure 25-Marcus curve in red and plotted ΔG° and kq with BIH as sacrificial donor for $[Ir(piq)_2(bpy)]^+$ (1), $[Ir(piq)_2(4,4'-(^tBu)_2-bpy)]^+$ (5), $[Ir(piq)_2(6,6'-(CH_3)_2-bpy)]^+$ (4), $[Ir(piq)_2(5,5'-(CH_3)_2-bpy)]^+$ (3), $[Ir(piq)_2(4,4'-(CH_3)_2-bpy)]^+$ (2), $[Ir(piq)_2(4,4'-(Br)_2-bpy)]^+$ (8), $[Ir(piq)_2(4,4'-(OCH_3)_2-bpy)]^+$ (7), $[Ir(piq)_2(biq)]^+$ (9) , $[Ir(piq)_2(4,4'-(C_9H_{19})_2-bpy)]^+$ (6), $[Ir(piq)_2(4,4'-(CF_3)_2-bpy)]^+$ (10) and $[Ir(piq)_2(bpz)]^+$ (11) in black

IV Conclusion

In this work, a series of eleven $[Ir(piq)_2(LL)]^+$ photosensitizers was synthesized via one common route that involved the synthesis of the $[Ir(piq)_2(\mu\text{-}Cl)]_2$ dimer that further reacted with the N^N ligand. All photosensitizers exhibited appreciable visible light absorption with molar absorption coefficients in the 5400-7900 $M^{-1}cm^{-1}$ range at 427-442 nm. Excited-state electron transfer with classical electron donors such as TEA, TEOA and BIH was investigated by steady-state excited-state quenching experiments in acetonitrile at ambient temperature. With TEA and TEOA, the quenching rate constants were low (~10^6 $M^{-1}s^{-1}$), but they reached diffusion limited values (1.9-7.1 x10^9 $M^{-1}s^{-1}$) when BIH was used. Steady-state illumination in the presence of BIH confirmed that excited-state electron transfer occurred. Compounds with electron withdrawing 2,2'-bipyridine analogues were less stable upon irradiation in the presence of BIH, but the other photosensitizers exhibited exceptional dark- and photostability. This stability is vital for photoreduction catalysis, such as solar fuel formation via proton or CO_2 reduction, as reductants with $E_{1/2}(L^{n/n-1})$ between –1.34V and –1.47 V vs NHE can be reversibly accumulated. Altogether, the results presented herein show promises for the development of robust photosensitizers for the formation of solar fuels.

The observation of a Marcus inverted region is rarely observed in the literature for diffusional excited-state electron transfer and should hence be considered carefully. A mentioned, further investigation, notably by time-resolved photoluminescence and transient absorption spectroscopy are required to unambiguously determine if the Marcus inverted region is observable in this case. Given the uncertainty on some of the measurements, we also believe that expanding the series of Ir(III) photosensitizers to reach ΔG values that are located on the parabola of (**Figure 25)**. Is necessary. To do this it would be necessary to synthetize new complexes located in these areas. Completing the curve could thus prove a Marcus Curve which to date is still lacking experimental proofs.

V Experimental part

Ethanol (≥99.9%, VWR), dichloromethane (≥99.9%, VWR), methanol (≥99.9%, VWR), tetrahydrofuran (≥99.9%, VWR), diethyl ether (≥99%, VWR), acetone (≥99.9%, VWR), ethyl acetate (≥99.9%, VWR), 2-ethoxyethanol (≥99%, Acros Organics), acetonitrile (≥99.9%, VWR), acetonitrile anhydrous (99.8%, Sigma Aldrich), $[NH_4][PF_6]$ (99%, Fluorochem), $NaBH_4$ powder (98+%, Acros Organics), KOH (≥98% p.a., Roth), CH_3I (99% stab. with copper, ThermoFischer), 2-phenylbenzimidazole (>98.0%, TCI), tetra-*n*-butylammonium hexafluorophosphate (97%, Fluorochem), triethanolamine (99+%, Acros Organics), triethylamine (99%, Acros Organics), $K_2S_2O_8$ (99+%, Acros Organics), iridium trichloride hydrate (53% Ir, Pressure Chemical), 1-phenylisoquinoline (98%, TCI), 2,2'-bipyridine (97%, Ambeed), 4,4'-$(CH_3)_2$-2,2'-bipyridine (98%, ArkPharm), 5,5'-$(CH_3)_2$-2,2'-bipyridine (98%, Sigma Aldrich), 6,6'-$(CH_3)_2$-2,2'-bipyridine (99%, Ambeed), 4,4'-$(^tBu)_2$-2,2'-bipyridine (98%, ArkPharm), 4,4'-$(C_9H_{19})_2$-2,2'-bipyridine (97%, Alfa Aesar), 4,4'-$(OCH_3)_2$-2,2'-bipyridine (97%, Sigma Aldrich), 4,4'-$(Br)_2$-2,2'-bipyridine (97%, TCI), 2,2'-biquinoline (98%, Ambeed), were purchased from commercial sources and used as received. $[Ir(piq)_2(\mu\text{-}Cl)]_2$ and BIH were synthesized according to published procedures.[55,56] Water was purified by a Millipore Milli-Q system. The precipitates were isolated by centrifugation at 4000 rpm for 3 min in a Hettich Universal 320 centrifuge.

Nuclear Magnetic Resonance. Characteristic ^1H NMR spectra were obtained at room temperature using a Bruker AM-300 (300 MHz) or a Bruker AM-500 (500 MHz) spectrometer at 23 °C. Solvent residual peaks were used as internal standards for ^1H (δ = 1.94 ppm for CD_3CN). For chemical shift referencing. NMR spectra were processed using MNOVA.

High-resolution mass spectrometry. HRMS spectra were recorded on a Q-Extractive orbitrap from ThermoFisher. Samples were ionized by electrospray ionization (ESI; capillary temperature = 250 °C, vaporizer temperature = 250 °C, and sheath gas flow rate = 20).

UV−Visible Absorption. UV−vis absorption spectra were recorded on a Shimadzu UV-1700 with 1 cm path length quartz cell.

Electrochemistry. Cyclic voltammetry was performed with an Autolab PGSTAT 100 potentiostat using a standard three-electrode-cell, *i.e.* a glassy carbon disk working electrode

(approximate area = 0.03 cm^2), a platinum wire counter electrode and an aqueous Ag/AgCl reference electrode (salt bridge: 3M KCl/saturated AgCl). Experiments were performed in dry 0.1 M tetrabutylammonium hexafluorophosphate acetonitrile electrolyte, and the samples were purged with argon before each measurement.

Steady-State Photoluminescence. Room temperature steady-state photoluminescence (PL) spectra were recorded on a Horiba Scientific-FL-1000 fluorimeter and were corrected by calibration of the instrument's response with a standard tungsten-halogen lamp. The photoluminescence intensity was integrated for 0.1 s at 1 nm resolution and averaged over 3 scans.

Time-Resolved Photoluminescence. Time-resolved PL data were acquired on a nitrogen dye laser with excitation cantered at 445 nm. Pulsed light excitation was achieved with a Photon Technology International (PTI) GL-301 dye laser that was pumped by a PTI GL-3300 nitrogen laser. The PL was detected by a Hamamatsu R928 PMT optically coupled to a ScienceTech Model 9010 monochromator terminated into a LeCroy Waverunner LT322 oscilloscope. Decays were monitored at the PL maximum and averaged over 180 scans. Nonradiative and radiative rate constants were calculated from the quantum yields, $\Phi = k_r/(k_r + k_{nr})$ and lifetimes, $\tau = 1/(k_r + k_{nr})$.

Stern-Volmer experiments. Excited-state quenching experiments were performed on a Varian Cary Eclipse spectrometer and the photoluminescence spectra were not corrected for the instrument's response. Typically, an Ir (III) solution with an absorbance of ~ 0.1 around 420-440 nm was prepared in acetonitrile. Various quencher solutions with concentration ranging from 0.05 to 0.5 M were prepared in the desired solvent also containing the Ir(III) photosensitizer with the same absorbance. The solutions were purged with argon for 30 minutes prior to the experiments. The desired quencher was gradually added to the solution of iridium photosensitizer and the excited-state quenching was monitored by steady-state photoluminescence. The decrease of photoluminescence was related to the concentration of quencher and the respective Stern-Volmer plots were extrapolated using the following equation:

$$\frac{\sum(PLI_0)}{\sum(PLI)} = 1 + K_{SV}[Q] = 1 + k_q\tau_0[Q]$$

Steady-State illumination. Ir (III) solutions with an absorbance of ~ 0.5 around 420-440 nm were prepared in acetonitrile. BIH was added to reach a concentration of 1 mM. The solutions were purged with argon for 30 minutes in the dark prior to being irradiated with a blue LED commercial strip for up to 15 minutes. UV-Vis spectra were recorded every 5

minutes. Reversibility of the excited-state reduction was assessed by adding an excess of sacrificial electron acceptor, $K_2S_2O_8$.

Synthesis of the Ir(III) photosensitizers. Ir(III) chloro-bridged dimer $[Ir(piq)_2\mu\text{-}Cl]_2$ (75mg, 58.9μmol) and the corresponding diimine ligand (147.25 μmol, 2.5 eq.) were placed in a sealed tube under argon atmosphere with 9 mL of MeOH/DCM 2:1 mixture. The reaction was heated at 60 °C for 24 hours. After reaction, the orange-red mixture was brought to room temperature. The DCM fraction was evaporated, and the resulting solution was treated with 10 mL of milliQ water and an excess of NH_4PF_6 was then added. The complex was isolated by centrifugation and was washed 3 times with milliQ water and 3 times with diethyl ether to give the desired complexes with yields that ranged from 57 to 82 %.

$[Ir(piq)_2(bpy)]^+.PF_6^-$ was obtained by using the synthetic procedure described above with 2,2'-bipyridine as diimine ligand (23 mg), to give an orange powder (84.8 mg, 80% yield). **^{1}H NMR** (500 MHz, CD_3CN) δ 9.04 – 8.99 (m, 2H), 8.54 (d, *J* = 8.2 Hz, 2H), 8.38 (d, *J* = 8.1 Hz, 2H), 8.11 (td, *J* = 7.9, 1.6 Hz, 2H), 8.04 – 7.92 (m, 2H), 7.87 (ddd, *J* = 5.5, 1.6, 0.8 Hz, 2H), 7.85 – 7.78 (m, 4H), 7.51 (d, *J* = 6.4 Hz, 2H), 7.46 (ddd, *J* = 7.7, 5.5, 1.2 Hz, 2H), 7.42 (dd, *J* = 6.5, 0.9 Hz, 2H), 7.18 – 7.05 (m, 2H), 6.88 (td, *J* = 7.4, 1.3 Hz, 2H), 6.31 (dd, *J* = 7.6, 1.3 Hz, 2H). **HRMS** (ESI) m/z calculated for $[C_{40}H_{28}N_4Ir - PF_6]^+$ = 755.19144; found 755.19152. NMR data are consistent with literature values.[57]

$[Ir(piq)_2(4,4'\text{-}(CH_3)_2\text{-}bpy)]^+.PF_6^-$ was obtained by using the synthetic procedure described above with 4,4'-dimethyl-2,2'-bipyridine as diimine ligand (27.1 mg), to give an orange powder (88.1 mg, 80% yield). **^{1}H NMR** (500 MHz, CD_3CN) δ 9.06 – 8.95 (m, 2H), 8.44 – 8.27 (m, 4H), 8.06 – 7.92 (m, 2H), 7.91 – 7.74 (m, 4H), 7.68 (d, *J* = 5.7 Hz, 2H), 7.50 (d, *J* = 6.4 Hz, 2H), 7.42 (dd, *J* = 6.5, 0.9 Hz, 2H), 7.28 (ddd, *J* = 5.6, 1.8, 0.8 Hz, 2H), 7.12 (ddd, *J* = 8.2, 7.3, 1.3 Hz, 2H), 6.87 (td, *J* = 7.4, 1.3 Hz, 2H), 6.32 – 6.30 (m, 2H), 2.51 (s, 6H). **HRMS** (ESI) m/z calculated for $[C_{42}H_{32}N_4Ir - PF_6]^+$ = 783.22274; found 783.22266. NMR data are consistent with literature values.[58]

$[Ir(piq)_2(5,5'\text{-}(CH_3)_2\text{-}bpy))]^+.PF_6^-$ was obtained by using the synthetic procedure described above with 5,5'-dimethyl-2,2'-bipyridine as diimine ligand (27.1 mg), to give an orange powder (78.1 mg, 71% yield). **^{1}H NMR** (500 MHz, CD_3CN) δ 9.08 – 8.98 (m, 2H), 8.37 (t, *J* = 8.1 Hz, 4H), 8.04 – 7.96 (m, 2H), 7.93 – 7.88 (m, 2H), 7.87 – 7.77 (m, 4H), 7.60 (d, *J* = 2.0 Hz, 2H), 7.51 (d, *J* = 6.4 Hz, 2H), 7.42 (d, *J* = 6.4 Hz, 2H), 7.13 (ddd, *J* = 8.3, 7.2, 1.4 Hz,

2H), 6.88 (td, *J* = 7.4, 1.3 Hz, 2H), 6.30 (dd, *J* = 7.7, 1.3 Hz, 2H), 2.14 (s, 6H). **HRMS** (ESI) m/z calculated for $[C_{42}H_{32}N_4Ir - PF_6]^+$ = 783.22274; found 783.22251. NMR data are consistent with literature values.[59]

$[Ir(piq)_2(6,6'\text{-}(CH_3)_2\text{-}bpy))]^+.PF_6^-$ was obtained by using the synthetic procedure described above with 6,6'-dimethyl-2,2'-bipyridine as diimine ligand (27.1 mg), to give an orange powder (84.3 mg, 77% yield). **^{1}H NMR** (500 MHz, CD_3CN) δ 9.01 – 8.89 (m, 2H), 8.29 (d, *J* = 7.5 Hz, 2H), 8.19 (d, *J* = 8.0 Hz, 2H), 8.04 – 7.97 (m, 2H), 7.91 (t, *J* = 7.9 Hz, 2H), 7.88 – 7.75 (m, 6H), 7.45 (d, *J* = 6.2 Hz, 2H), 7.29 (dd, *J* = 7.7, 1.2 Hz, 2H), 7.03 (ddd, *J* = 8.3, 7.2, 1.3 Hz, 2H), 6.81 – 6.61 (m, 2H), 6.30 (dd, *J* = 7.7, 1.3 Hz, 2H), 1.81 (s, 6H). **HRMS** (ESI) m/z calculated for $[C_{42}H_{32}N_4Ir - PF_6]^+$ = 783.22274; found 783.22256.

$[Ir(piq)_2(4,4'\text{-}(^t Bu)_2\text{-}bpy))]^+.PF_6^-$ was obtained by using the synthetic procedure described above with 4,4'-^{t}Bu-2,2'-bipyridine as diimine ligand (39.5 mg), to give an orange powder (68.6 mg, 57% yield). **^{1}H NMR** (500 MHz, CD_3CN) δ 9.07 – 8.95 (m, 2H), 8.52 (dd, *J* = 2.1, 0.7 Hz, 2H), 8.37 (d, *J* = 8.0 Hz, 2H), 8.08 – 7.93 (m, 2H), 7.89 – 7.79 (m, 4H), 7.73 (dd, *J* = 5.9, 0.6 Hz, 2H), 7.55 – 7.36 (m, 6H), 7.12 (ddd, *J* = 8.1, 7.2, 1.3 Hz, 2H), 6.87 (td, *J* = 7.4, 1.2 Hz, 2H), 6.30 (dd, *J* = 8.0, 1.3 Hz, 2H), 1.39 (s, 18H). **HRMS** (ESI) m/z calculated for $[C_{48}H_{44}N_4Ir - PF_6]^+$ = 867.31664; found 867.31621. NMR data are consistent with literature values.[60]

$[Ir(piq)_2(4,4'\text{-}(C_9H_{19})_2\text{-}bpy))]^+.PF_6^-$ was obtained by using the synthetic procedure described above with 4,4'-$CH_3(CH_2)_8$-2,2'-bipyridine as diimine ligand (60.1 mg), to give an orange powder (81.3 mg, 60% yield). **^{1}H NMR** (500 MHz, CD_3CN) δ 9.01 (dd, *J* = 6.4, 3.4 Hz, 2H), 8.48 – 8.30 (m, 4H), 8.07 – 7.93 (m, 2H), 7.90 – 7.74 (m, 4H), 7.69 (d, *J* = 5.9 Hz, 2H), 7.49 (d, *J* = 6.5 Hz, 2H), 7.42 (d, *J* = 5.9 Hz, 2H), 7.28 (dd, *J* = 5.7, 1.9 Hz, 2H), 7.17 – 7.05 (m, 2H), 6.87 (td, *J* = 7.4, 1.3 Hz, 2H), 6.31 (dd, *J* = 7.7, 1.4 Hz, 2H), 2.78 (t, *J* = 7.7 Hz, 4H), 1.69 (q, *J* = 7.2 Hz, 4H), 1.45 – 1.09 (m, 24H), 0.99 – 0.68 (m, 6H). **HRMS** (ESI) m/z calculated for $[C_{58}H_{64}N_4Ir - PF_6]^+$ = 1007.47314; found 1007.47317. NMR data are consistent with literature values.[61]

$[Ir(piq)_2(4,4'\text{-}(OCH_3)_2\text{-}bpy)MeO\text{-}bpy)]^+.PF_6^-$ was obtained by using the synthetic procedure described above with 4,4'-MeO-2,2'-bipyridine as diimine ligand (31.8 mg), to give an orange powder (93.4 mg, 82% yield). **^{1}H NMR** (500 MHz, CD_3CN) δ 9.07 – 8.92 (m, 2H), 8.36 (d, *J* = 8.0 Hz, 2H), 8.00 (dd, *J* = 6.8, 2.7 Hz, 4H), 7.92 – 7.72 (m, 4H), 7.61 (d, *J* = 6.4

Hz, 2H), 7.56 (d, *J* = 6.5 Hz, 2H), 7.45 (d, *J* = 6.3 Hz, 2H), 7.16 – 7.06 (m, 2H), 6.98 (dd, *J* = 6.4, 2.7 Hz, 2H), 6.86 (td, *J* = 7.4, 1.3 Hz, 2H), 6.31 (dd, *J* = 7.9, 1.1 Hz, 2H), 3.97 (s, 6H). **HRMS** (ESI) m/z calculated for $[C_{42}H_{32}O_2N_4Ir - PF_6]^+$ = 815.21257; found 815.21250. NMR data are consistent with literature values.[62]

$[Ir(piq)_2(4,4'\text{-}(Br)_2\text{-}bpy)]^+.PF_6^-$ was obtained by using the synthetic procedure described above with 4,4'-Br-2,2'-bipyridine as diimine ligand (45.9 mg), to give a red powder (86.3 mg, 70% yield). **^{1}H NMR** (500 MHz, CD_3CN) δ 9.08 – 8.95 (m, 2H), 8.79 (dd, *J* = 1.7, 0.9 Hz, 2H), 8.52 – 8.29 (m, 2H), 8.04 – 7.97 (m, 2H), 7.90 – 7.79 (m, 4H), 7.66 (t, *J* = 1.1 Hz, 4H), 7.51 (d, *J* = 6.4 Hz, 2H), 7.48 – 7.42 (m, 2H), 7.13 (ddd, *J* = 8.2, 7.3, 1.3 Hz, 2H), 6.88 (td, *J* = 7.5, 1.3 Hz, 2H), 6.26 (dd, *J* = 7.7, 1.3 Hz, 2H). **HRMS** (ESI) m/z calculated for $[C_{40}H_{26}N_4Br_2Ir - PF_6]^+$ = 911.01246; found 911.01276.

$[Ir(piq)_2(biq)]^+.PF_6^-$ was obtained by using the synthetic procedure described above with 2,2'-biquinoline as diimine ligand (37.7 mg), to give a dark purple powder (96.2 mg, 81% yield). **^{1}H NMR** (500 MHz, CD_3CN) δ 8.82 (d, *J* = 8.8 Hz, 2H), 8.65 (d, *J* = 8.7 Hz, 2H), 8.56 (d, *J* = 8.8 Hz, 2H), 8.27 (d, *J* = 7.4 Hz, 2H), 8.00 – 7.89 (m, 4H), 7.86 – 7.70 (m, 8H), 7.53 (ddd, *J* = 8.1, 6.8, 1.1 Hz, 2H), 7.31 (d, *J* = 6.5 Hz, 2H), 7.14 (ddd, *J* = 8.7, 6.8, 1.5 Hz, 2H), 7.10 (ddd, *J* = 8.2, 7.2, 1.3 Hz, 2H), 6.87 (td, *J* = 7.4, 1.3 Hz, 2H), 6.47 (dd, *J* = 7.8, 1.4 Hz, 2H). **HRMS** (ESI) m/z calculated for $[C_{48}H_{32}N_4Ir - PF_6]^+$ = 855.22274; found 855.22281. NMR data are consistent with literature values.[63]

VI Bibliographical references

[1] Morgan, J; (2016). Paris COP 21: Power that speaks the truth?. Globalizations, 13(6), 943-951. https://doi.org/10.1080/14747731.2016.1163863

[2] Masson-Delmotte, V.; Zhai, P.; Pörtner, H. O.; Roberts, D.; Skea, J.; & Shukla, P. R. (2022). Global Warming of 1.5 C: IPCC special report on impacts of global warming of 1.5 C above pre-industrial levels in context of strengthening response to climate change, sustainable development, and efforts to eradicate poverty. Cambridge University Press. https://doi.org/10.1017/9781009157940

[3] Council, H; (2021). McKinsey & Company, Hydrogen Insights Report (2021).

[4] Palo, D. R., Dagle, R. A., & Holladay, J. D. (2007). Methanol steam reforming for hydrogen production. Chemical reviews, 107(10), 3992-4021. https://doi.org/10.1021/cr050198b

[5] Martavaltzi, C; S., Pampaka, E. P.; Korkakaki, E. S.; & Lemonidou, A. A. (2010). Hydrogen production via steam reforming of methane with simultaneous CO2 capture over CaO− Ca12Al14O33. Energy & Fuels, 24(4), 2589-2595. https://doi.org/10.1021/ef9014058

[6] El-Shafie, M.; Kambara, S.; Hayakawa, Y. (2019). Hydrogen production technologies overview. Journal of Power and Energy Engineering, https://doi.org/10.4236/jpee.2019.71007

[7] Chi, J., & Yu, H. (2018). Water electrolysis based on renewable energy for hydrogen production. Chinese Journal of Catalysis, 39(3), 390-394. https://doi.org/10.1016/S1872-2067(17)62949-8

[8] Midilli, A.; Kucuk, H.; Topal, M. E.; Akbulut, U.; & Dincer, I. (2021). A comprehensive review on hydrogen production from coal gasification: Challenges and Opportunities. International Journal of Hydrogen Energy, 46(50), 25385-25412. https://doi.org/10.1016/j.ijhydene.2021.05.088

[9] Ni, M.; Leung, D. Y. ; Leung, M. K. ; & Sumathy, K. J. F. P. T. (2006). An overview of hydrogen production from biomass. Fuel processing technology, 87(5), 461-472. https://doi.org/10.1016/j.fuproc.2005.11.003

[10] Newborough, M.; & Cooley, G. (2020). Developments in the global hydrogen market: The spectrum of hydrogen colours. Fuel Cells Bulletin, 2020(11), 16-22. https://doi.org/10.1016/S1464-2859(20)30546-0

[11] Vander Wee-Leonard, M; Light-induced halides oxidation in water with iridium complexes for HX splitting; Presented in the name of PhD Student's day, Friday 26th of may 2023, Louvain-la-Neuve, Belgium

[12] Vinoth Kanna, I.; & Paturu, P. (2020). A study of hydrogen as an alternative fuel. International Journal of Ambient Energy, 41(12), 1433-1436. https://doi.org/10.1080/01430750.2018.1484803

[13] Ramesohl, S.; & Merten, F. (2006). Energy system aspects of hydrogen as an alternative fuel in transport. Energy policy, 34(11), 1251-1259. https://doi.org/10.1016/j.enpol.2005.12.018

[14] Johnston, B.; Mayo, M. C.; & Khare, A. (2005). Hydrogen: the energy source for the 21st century. Technovation, 25(6), 569-585. https://doi.org/10.1016/j.technovation.2003.11.005

[15] Gerboni, R. (2016). Introduction to hydrogen transportation. In Compendium of hydrogen energy (pp. 283-299). Woodhead Publishing. https://doi.org/10.1016/B978-1-78242-362-1.00011-0

[16] Moreira, S.; & Laing, T. J. (2022). Sufficiency, sustainability, and circularity of critical materials for clean hydrogen. http://hdl.handle.net/10986/38413

[17] Alzahrani, A.; Ramu, S.K.; Devarajan, G.; Vairavasundaram, I.; Vairavasundaram, S. A Review on Hydrogen-Based Hybrid Microgrid System: Topologies for Hydrogen Energy Storage, Integration, and Energy Management with Solar and Wind Energy. Energies 2022, 15, 7979, https://doi.org/10.3390/en15217979

[18] Dervisogly, R. Fuel Cell. Available online: https://en.wikipedia.org/wiki/Fuel_cell (accessed on 25 April 2023).

[19] Les premiers TER hydrogène dans vos gares d'ici 2025. Available online: https://www.sncf.com/fr/engagements/enjeux-rse/sncf-accelere-train-a-hydrogene (accessed on 21 March 2023).

[20] Executive summary. Available online: https://www.iea.org/reports/renewables-2022/executive-summary (accessed on 21 March 2023)

[21] nuGen, decarbonising Anglo American our planet. Building a cleaner, greener and more sustainable world. Available online: https://southafrica.angloamerican.com/our-difference/futuresmart-mining/nugen (accessed on 22 March 2023)

[22] Hydrogen technologies faces efficiency disadvantage in power storage race. Available online: https://www.spglobal.com/marketintelligence/en/news-insights/latest-news-headlines/hydrogen-technology-faces-efficiency-disadvantage-in-power-storage-race-65162028 (accessed on 22 March 2023)

[23] IEA World energy balance. Available online: https://www.iea.org/reports/world-energy-balances-overview/world (accessed on 18 March 2023)

[24] Esswein, A. J. ; & Nocera, D. G. (2007). Hydrogen production by molecular photocatalysis. Chemical reviews, 107(10), 4022-4047. https://doi.org/10.1021/cr050193e

[25] Ozawa, H.; Haga, M. A., & Sakai, K. (2006). A photo-hydrogen-evolving molecular device driving visible-light-induced EDTA-reduction of water into molecular hydrogen. Journal of the American Chemical Society, 128(15), 4926-4927. https://doi.org/10.1021/ja058087h

[26] Arachchige, S. M.; Brown, J. R.; Chang, E.; Jain, A.; Zigler, D. F.; Rangan, K., & Brewer, K. J. (2009). Design considerations for a system for photocatalytic hydrogen production from water employing mixed-metal photochemical molecular devices for photoinitiated electron collection. Inorganic chemistry, 48(5), 1989-2000. https://doi.org/10.1021/ic8017387

[27] Whang, D. R.; Sakai, K.; & Park, S. Y. (2013). Highly efficient photocatalytic water reduction with robust iridium (III) photosensitizers containing arylsilyl substituents. Angewandte Chemie International Edition, 52(44), 11612-11615. https://doi.org/10.1002/anie.201305684

[28] Kobayashi, M. ; Masaoka, S. ; & Sakai, K. (2012). Photoinduced hydrogen evolution from water by a simple platinum (II) terpyridine derivative: a Z-scheme photosynthesis. Angewandte Chemie-International Edition, 51(30), 7431-7434. https://doi.org/10.1002/anie.201202720

[29] Lentz, C; (2018) Photophysics and photochemistry of trischelate Ir(III) complexes: towards development of novel photoactive supramolecules.

[30] Xie, A.; Liu, X. L.; Xiang, Y. C.; Luo, G. G. (2017). A homogeneous molecular system for the photogeneration of hydrogen from water based on a [RuII (bpy) 3] 2+ photosensitizer and a phthalycyanine cobalt catalyst. Journal of Alloys and Compounds, 717, 226-231, https://doi.org/10.1016/j.jallcom.2017.05.040.

[31] Pellegrin, Y.; & Odobel, F. (2017). Sacrificial electron donor reagents for solar fuel production. Comptes Rendus Chimie, 20(3), 283-295. https://doi.org/10.1016/j.crci.2015.11.026

[32] Molecular orbital. Available online: https://ch301.cm.utexas.edu/imfs/#mo/mo-theory-all.php (accessed on 27 April 2023).

[33] Hood, S. T.; Hamnett, A.; & Brion, C. E. (1977). Molecular orbital momentum distributions and binding energies for H2O using an electron impact coincidence spectrometer. Journal of Electron Spectroscopy and Related Phenomena, 11(2), 205-224. https://doi.org/10.1016/0368-2048(77)85111-6

[34] Bevernaegie, R. (2019). Development of iridium-based sensitizers for oxygen-independent phototherapy and solar energy conversion.

[35] Deaton, J. C.; & Castellano, F. N. (2017). Archetypal iridium (III) compounds for optoelectronic and photonic applications: photophysical properties and synthetic methods. Iridium (III) in optoelectronic and photonics applications, 1-69. https://doi.org/10.1002/9781119007166.ch1

[36] What is a Jablonsky diagram (Perrin-Jablonski diagram)?. Available online: https://www.edinst.com/de/blog/jablonski-diagram/ (accessed on 27 April 2023).

[37] Piechota, E. J.; Meyer, G. J. (2019). Introduction to electron transfer: Theoretical foundations and pedagogical examples. Journal of Chemical Education, 96(11), 2450-2466, https://doi.org/10.1021/acs.jchemed.9b00489

[38] Closs, G. L.; Miller, J. R. (1988). Intramolecular long-distance electron transfer in organic molecules. Science, 240(4851), 440-447, https://doi.org/10.1126/science.240.4851.440

[39] Wodon, M.; De Kreijger, S.; Sampaio, R. N.; Elias, B.; Troian-Gautier, L. (2022). Accumulation of mono-reduced [Ir (piq) 2 (LL)] photosensitizers relevant for solar fuels production. Photochemical & Photobiological Sciences, 21(8), 1433-1444, https://doi.org/10.1007/s43630-022-00233-z.

[40] Bevernaegie, R.; Wehlin, S. A. M.; Elias, B.; Troian-Gautier, L. (2021). A Roadmap Towards Visible Light Mediated Electron Transfer Chemistry with Iridium(III) Complexes. ChemPhotoChem 5, 217-234, https://doi.org/10.1002/cptc.202000255.

[41] Nonoyama, M. (1974). Benzo[h]quinolin-10-yl-N Iridium(III) Complexes. Bulletin of the Chemical Society of Japan 47, 767-768, https://doi.org/10.1246/bcsj.47.767.

[42] Bevernaegie, R.; Marcélis, L.; Moreno-Betancourt, A.; Laramée-Milette, B.; Hanan, G. S.; Loiseau, F.; Sliwa, M.; Elias, B. (2018). Ultrafast charge transfer excited state dynamics in trifluoromethyl-substituted iridium(iii) complexes. Physical Chemistry Chemical Physics 20, 27256-27260, https://doi.org/10.1039/C8CP04265A.

[43] Bevernaegie, R.; Marcélis, L.; Laramée-Milette, B.; De Winter, J.; Robeyns, K.; Gerbaux, P.; Hanan, G. S.; Elias, B. (2018). Trifluoromethyl-Substituted Iridium(III) Complexes: From Photophysics to Photooxidation of a Biological Target. Inorganic Chemistry 57, 1356-1367, https://doi.org/10.1021/acs.inorgchem.7b02778.

[44] Brouwer, A. M. (2011). Standards for photoluminescence quantum yield measurements in solution (IUPAC Technical Report). Pure and Applied Chemistry 83, 2213-2228, https://doi.org/doi:10.1351/PAC-REP-10-09-31.

[45] Juris, A.; Balzani, V.; Barigelletti, F.; Campagna, S.; Belser, P.; von Zelewsky, A. (1988). Ru(II) polypyridine complexes: photophysics, photochemistry, eletrochemistry, and chemiluminescence. Coordination Chemistry Reviews 84, 85-277, https://doi.org/https://doi.org/10.1016/0010-8545(88)80032-8.

[46] Campagna, S.; Puntoriero, F.; Nastasi, F.; Bergamini, G.; Balzani, V., Photochemistry and Photophysics of Coordination Compounds: Ruthenium. In Photochemistry and Photophysics of Coordination Compounds I, Balzani, V.; Campagna, S., Eds. Springer Berlin Heidelberg: Berlin, Heidelberg, 2007; pp 117-214.

[47] Yarnell, J. E.; McCusker, C. E.; Leeds, A. J.; Breaux, J. M.; Castellano, F. N. (2016). Exposing the Excited-State Equilibrium in an IrIII Bichromophore: A Combined Time Resolved Spectroscopy and Computational Study. European Journal of Inorganic Chemistry 2016, 1808-1818, https://doi.org/https://doi.org/10.1002/ejic.201600194.

[48] McCusker, C. E.; Chakraborty, A.; Castellano, F. N. (2014). Excited State Equilibrium Induced Lifetime Extension in a Dinuclear Platinum(II) Complex. The Journal of Physical Chemistry A 118, 10391-10399, https://doi.org/10.1021/jp503827e.

[49] Aydogan, A.; Bangle, R. E.; De Kreijger, S.; Dickenson, J. C.; Singleton, M. L.; Cauët, E.; Cadranel, A.; Meyer, G. J.; Elias, B.; Sampaio, R. N.; Troian-Gautier, L. (2021). Mechanistic investigation of a visible light mediated dehalogenation/cyclisation reaction using iron(iii), iridium(iii) and ruthenium(ii) photosensitizers. Catalysis Science & Technology 11, 8037-8051, https://doi.org/10.1039/D1CY01771C.

[50] Connell, T. U.; Fraser, C. L.; Czyz, M. L.; Smith, Z. M.; Hayne, D. J.; Doeven, E. H.; Agugiaro, J.; Wilson, D. J. D.; Adcock, J. L.; Scully, A. D.; Gómez, D. E.; Barnett, N. W.; Polyzos, A.; Francis, P. S. (2019). The Tandem Photoredox Catalysis Mechanism of [Ir(ppy)2(dtb-bpy)]+ Enabling Access to Energy Demanding Organic Substrates. Journal of the American Chemical Society 141, 17646-17658, https://doi.org/10.1021/jacs.9b07370.

[51] Takeda, N.; Miller, J. R. (2020). Inverted Region in Bimolecular Electron Transfer in Solution Enabled by Delocalization. Journal of the American Chemical Society 142, 17997-18004, https://doi.org/10.1021/jacs.0c04780.

[52] Bevernaegie, R.; Wehlin, S. A. M.; Piechota, E. J.; Abraham, M.; Philouze, C.; Meyer, G. J.; Elias, B.; Troian-Gautier, L. (2020). Improved Visible Light Absorption of Potent Iridium(III) Photo-oxidants for Excited-State Electron Transfer Chemistry. Journal of the American Chemical Society 142, 2732-2737, https://doi.org/10.1021/jacs.9b12108.

[53] Piechota, E. J.; Meyer, G. J. (2019). Introduction to Electron Transfer: Theoretical Foundations and Pedagogical Examples. Journal of Chemical Education 96, 2450-2466, https://doi.org/10.1021/acs.jchemed.9b00489.

[54] Closs, G. L.; Miller, J. R. (1988). Intramolecular Long-Distance Electron Transfer in Organic Molecules. Science 240, 440-447, https://doi.org/doi:10.1126/science.240.4851.440.

[55] Sampaio, R. N.; Grills, D. C.; Polyansky, D. E.; Szalda, D. J.; Fujita, E. (2020). Unexpected Roles of Triethanolamine in the Photochemical Reduction of CO2 to Formate by Ruthenium Complexes. Journal of the American Chemical Society 142, 2413-2428, https://doi.org/10.1021/jacs.9b11897.

[56] Nonoyama, M. (1974). Benzo[h]quinolin-10-yl-N Iridium(III) Complexes. Bulletin of the Chemical Society of Japan 47, 767-768, https://doi.org/10.1246/bcsj.47.767.

[57] Lentz, C.; Schott, O.; Auvray, T.; Hanan, G.; Elias, B. (2017). Photocatalytic Hydrogen Production Using a Red-Absorbing Ir(III)–Co(III) Dyad. Inorganic Chemistry 56, 10875-10881, https://doi.org/10.1021/acs.inorgchem.7b00684.

[58] Sauvageot, E.; Lafite, P.; Duverger, E.; Marion, R.; Hamel, M.; Gaillard, S.; Renaud, J.-L.; Daniellou, R. (2016). Iridium complexes inhibit tumor necrosis factor-α by utilizing light and mixed ligands. Journal of Organometallic Chemistry 808, 122-127, https://doi.org/https://doi.org/10.1016/j.jorganchem.2016.02.001.

[59] Lin, S.; Gao, W.; Tian, Z.; Yang, C.; Lu, L.; Mergny, J.-L.; Leung, C.-H.; Ma, D.-L. (2015). Luminescence switch-on detection of protein tyrosine kinase-7 using a G-quadruplex-selective probe. Chemical Science 6, 4284-4290, https://doi.org/10.1039/C5SC01320H.

[60] Lu, L.; Shiu-Hin Chan, D.; Kwong, D. W. J.; He, H.-Z.; Leung, C.-H.; Ma, D.-L. (2014). Detection of nicking endonuclease activity using a G-quadruplex-selective luminescent switch-on probe. Chemical Science 5, 4561-4568, https://doi.org/10.1039/C4SC02032D.

[61] Lin, S.; He, B.; Yang, C.; Leung, C.-H.; Mergny, J.-L.; Ma, D.-L. (2015). Luminescence switch-on assay of interferon-gamma using a G-quadruplex-selective iridium(iii) complex. Chemical Communications 51, 16033-16036, https://doi.org/10.1039/C5CC06655G.

[62] Liu, L.-J.; Lu, L.; Zhong, H.-J.; He, B.; Kwong, D. W. J.; Ma, D.-L.; Leung, C.-H. (2015). An Iridium(III) Complex Inhibits JMJD2 Activities and Acts as a Potential Epigenetic Modulator. Journal of Medicinal Chemistry 58, 6697-6703, https://doi.org/10.1021/acs.jmedchem.5b00375.

[63] Zhao, Q.; Liu, S.; Shi, M.; Wang, C.; Yu, M.; Li, L.; Li, F.; Yi, T.; Huang, C. (2006). Series of New Cationic Iridium(III) Complexes with Tunable Emission Wavelength and Excited State Properties: Structures, Theoretical Calculations, and Photophysical and Electrochemical Properties. Inorganic Chemistry 45, 6152-6160, https://doi.org/10.1021/ic052034j.

Accumulation of Mono-Reduced $[Ir(piq)_2(LL)]^+$ Photosensitizers Relevant for Solar Fuels Productions

A series of nine $[Ir(piq)_2(LL)]^+.PF_6^-$ photosensitizers were developed and investigated for excited-state electron transfer with sacrificial electron donors that included triethanolamine (TEOA), triethylamine (TEA), and 1,3-dimethyl-2-phenyl-2,3-dihydro-1*H*-benzo[*d*]imidazole (BIH) in acetonitrile. The photosensitizers were obtained in 57-82% yield starting from the common $[Ir(piq)_2Cl]_2$ precursor and were all characterized by UV-Vis absorption as well as by steady-state, time-resolved spectroscopies, and electrochemistry. The excited-state lifetimes ranged from 250 to 3350 ns and were also shown, in some cases, to be strongly influenced by dissolved oxygen. Excited-state electron transfer quenching rate constants in the 10 $M^{-1}s^{-1}$ range were obtained when BIH was used as electron donor. These quenching rate constants were three orders of magnitude higher than when TEA or TEOA is used. Steady-state photolysis in the presence of BIH showed that the stable and reversible accumulation of mono-reduced photosensitizers was possible, highlighting the potential use of these Ir-based photosensitizers in photocatalytic reactions relevant for solar fuels production.

Auteur: Martin Wodon

UNIVERSITE CATHOLIQUE DE LOUVAIN

Faculté bioingénieurs

Croix du sud, 2 bte L7.05.01, 1348 Louvain-la-Neuve, Belgique I **www.uclouvain.be/agro**